Earth Planet. Sci. Lett. 671 (2025) 119621

Contents lists available at ScienceDirect

Earth and Planetary Science Letters

journal homepage: www.elsevier.com/locate/epsl

Evolution of iron formation to ore during Ediacaran to early Paleozoic tectonic stability

Anthony J. Fuentes [a,*], Liam Courtney-Davies [b], Rebecca Flowers [b], Yiming Zhang [a,c], Nicholas Swanson-Hysell [a,c]

[a] Department of Earth and Planetary Science, University of California Berkeley, 307 McCone Hall, Berkeley, 94702, CA, USA
[b] Department of Geological Sciences, University of Colorado Boulder, UCB 399, Boulder, 80309, CO, USA
[c] Institute for Rock Magnetism, Department of Earth and Environmental Sciences, University of Minnesota, 150 John T. Tate Hall, 116 Church St. SE, Minneapolis, 55455, MN, USA

ARTICLE INFO

Editor: A. Webb

Dataset link: https://github.com/Swanson-Hysell-Group/Negaunee_Goodrich, https://doi.org/10.7288/V4/MAGIC/20184, https://doi.org/10.5281/zenodo.13883216

Keywords:
Banded iron formation
Oxidation
Iron ore
Proterozoic
Hematite U-Pb geochronology

ABSTRACT

The enrichment of iron formation (IF) to form economically important hematitic iron ore has been linked to a range of mechanisms from interactions with hydrothermal or metamorphic fluids during active tectonics to chemical leaching driven by meteoric water in the very near surface. Direct geochronologic constraints on hematite that can link ore-forming processes to geologic events have only recently become possible. Here, we present spatially resolved hematite U-Pb and paleomagnetic data for Paleoproterozoic IF, and associated hematite ore bodies from Northern Michigan, USA, to assess the timing of hematite crystallization in these units. Our paired paleomagnetic and radiometric dating approach indicates that hematite crystallization in different iron oxide facies spanned the Proterozoic into the early Paleozoic. Notably, hematite ore enrichment occurred during a period of regional tectonic quiescence in the latest Neoproterozoic and early Paleozoic. At this time, Laurentia was at tropical paleolatitudes and for much of this interval Earth was in a particularly warm non-glacial interval. These results indicate that the hematite ore at the study locality developed through supergene process via the interaction of the host IF with warm meteoric water transported downward to the subsurface rather than hypogene hydrothermal fluids linked to tectonism in the Paleoproterozoic.

1. Introduction

Despite the economic importance and widespread interest in understanding the encoded paleoenvironmental information in iron formation (IF), the timing of iron oxide crystallization within these units and associated ore bodies remains unclear or contested in many settings. A major difficulty in determining the age of ore crystallization is the paucity of phases that have traditionally been dateable in these lithologies (Hagemann et al., 2006; Konhauser et al., 2017; Robbins et al., 2019; Rasmussen et al., 2021). Consequently, there are open questions about the tectonic setting and suite of processes that led to hematite enrichment during ore formation. The development of concentrated hematite bodies necessitates large volumes of fluids with broadly two categories of hypotheses around the genesis and nature of those fluids (Evans et al., 2013; Hagemann et al., 2016). Both enrichment regimes require the progressive leaching of silica, in addition to authigenic iron oxide crystallization, through interactions with structurally mediated fluids that results in the progressive enrichment of iron oxides at the expense of silica in the host-IF. The first category invokes hypogene enrichment during orogenesis or rifting by metamorphic or hydrothermal fluids that migrate upward from the deep subsurface through fractures or fault conduits (Figueiredo e Silva et al., 2013; Keyser et al., 2019; Angerer et al., 2022). In contrast, supergene enrichment implicates downward migrating meteoric water as the catalyst for iron ore formation (Morris and Wolff, 1985). Supergene enrichment processes include either lateritic weathering in a surface weathering profile or deeper seated supergene mimetic enrichment (Ramanaidou and Morris, 2010). Lateritic weathering typically obliterates textures and results in the formation of goethite (Ramanaidou and Morris, 2010). In contrast, mimetic enrichment can result from descending groundwater and can preserve relicts of primary textures (Ramanaidou and Morris, 2010). However, iron ore genesis has the potential to be a complex, polyphase process with contributions from

* Corresponding author.
E-mail addresses: anthony.j.fuentes@berkeley.edu (A.J. Fuentes), Liam.Courtney-Davies@colorado.edu (L. Courtney-Davies), rebecca.flowers@colorado.edu (R. Flowers), yiming-z@umn.edu (Y. Zhang), nicks-h@umn.edu (N. Swanson-Hysell).

https://doi.org/10.1016/j.epsl.2025.119621
Received 14 November 2024; Received in revised form 22 July 2025; Accepted 3 September 2025

Available online 16 September 2025

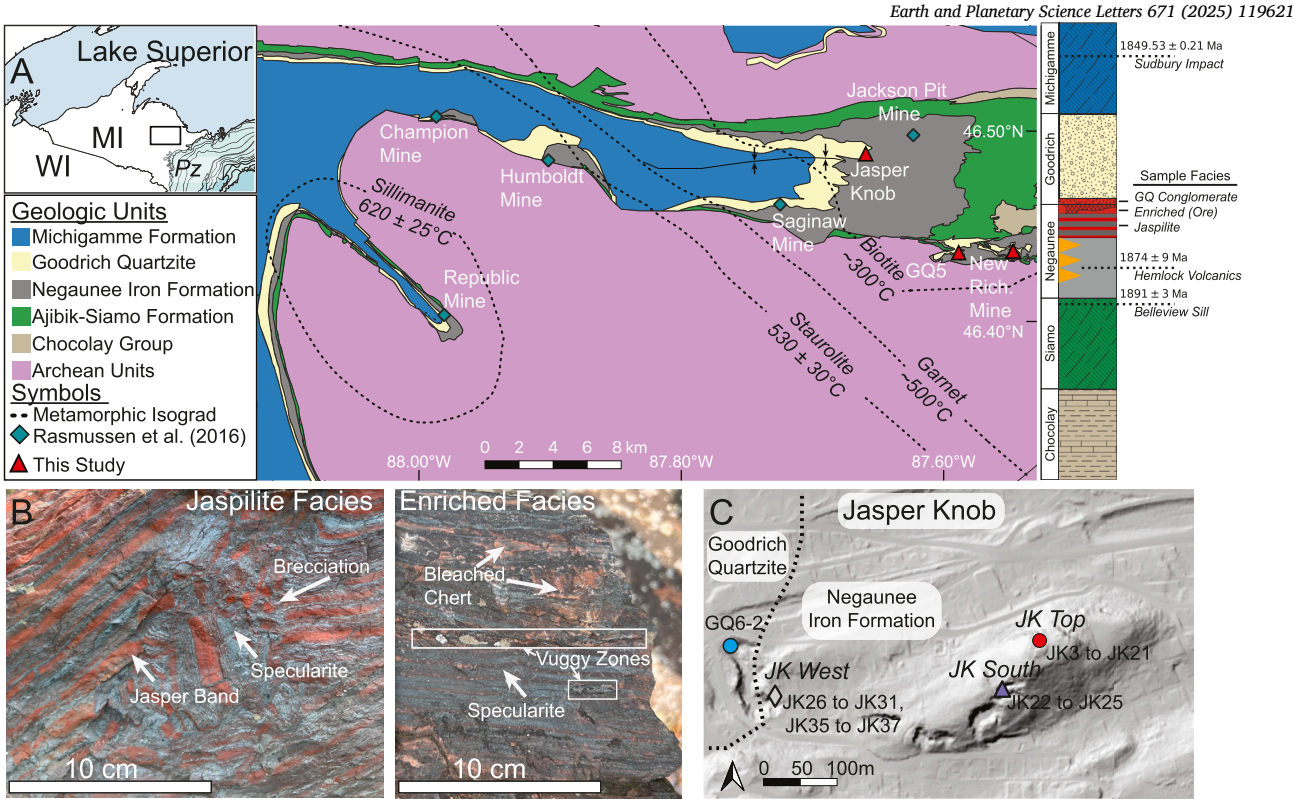

Fig. 1. *(A)* Simplified regional geologic map modified from refs (Puffett, 1974; Cannon and Klasner, 1976; Gair and Han, 1975; Simmons, 1974; Cannon and Klasner, 1977) of the Marquette syncline that is composed predominantly of units from the Marquette Range Supergroup. Dashed black lines are metamorphic isograds and estimated metamorphic temperatures based upon mineral assemblages (Haase, 1982; Tohver et al., 2007). Light blue diamonds are the sampled locations for the monazite and xenotime U-Pb dates reported by ref. (Rasmussen et al., 2016) and red triangles correspond to sampling locations for this study. The stratigraphic column of the map units is shown to the right of the map. Dashed lines are the existing age constraints on the deposition of the Negaunee and Goodrich, including the Hemlock Volcanics that are laterally correlative to the Negaunee (Schneider et al., 2002; Davis, 2008; Pietrzak-Renaud and Davis, 2014, orange). Solid black lines with labels designate the three facies sampled for paleomagnetism and geochronology. Inset map of the study region shows the mapped extent of Paleozoic sedimentary rocks deposited during Paleozoic transgressions (Pz). *(B)* Field photos showing the jaspilite facies and enriched iron formation facies (sample JK22) from the south side of Jasper Knob. *(C)* A LiDAR-derived hillshade of Jasper Knob illustrating the spatial relationships between the jaspilite samples (JK Top), enriched iron formation samples (JK South), variable enriched iron formation samples (JK West), and dated sample in the Goodrich Quartzite (GQ-6). The enriched facies samples are on the margin of historically mined ore deposits with pits visible along the western and southern portion of the hillshade image.

both hypogene and supergene mechanisms. Thus, the absence of direct chronological data on hematite crystallization across different oxide textures has made it difficult to confidently link hematite enrichment with specific events and processes (Powell et al., 1999; Courtney-Davies et al., 2024).

Establishing temporal constraints on iron mineralization has largely focused on U-Pb dating of accessory phases like monazite and xenotime (Rasmussen et al., 2007; Santos et al., 2010; Dukino et al., 2000). This approach has been applied to ore hosted by the Negaunee Iron Formation and Goodrich Quartzite of the Marquette Range Supergroup, which has led to the interpretation that all hematite enrichment in the region is synorogenic and associated with Paleoproterozoic orogenesis (Rasmussen et al., 2016). However, the hematitic ore deposits spanning these units have a range of expressions, from highly schistose ore adjacent to shear zones that experienced the most intense metamorphism, to deposits that preserve banded textures such as those observed at Jasper Knob and the New Richmond mine (Fig. 1), and show ambiguous affinity to specific orogenic events. The monazite and xenotime ages from the Negaunee and Goodrich ore deposits are from the highly sheared schistose ore, leading to the interpretation that the hematite ore is soley associated with three discrete upgrading events during the Paleoproterozoic Penokean and Yavapai orogenies (Rasmussen et al., 2016). While the crenulated texture of the schistose hematite ore is consistent with a metamorphic origin for those deposits, the diverse textural characteristics of the hematite ore bodies may imply a more complex and protracted history of ore enrichment.

Advances in hematite U-Pb geochronology, such as the development of a hematite-specific reference material (Courtney-Davies et al., 2020), facilitates direct *in situ* determination of the age of hematite crystallization through Laser Ablation Inductively Coupled Plasma Mass Spectrometry (LA-ICP-MS) on different hematite textures in IFs (e.g., Courtney-Davies et al., 2024). Paleomagnetic data also have the potential to yield chronologic insights into hematite crystallization. As hematite crystals grow above ~30 nm, they become stable single domain particles that record magnetization from the time of growth (crystallization remanent magnetization (CRM); Özdemir and Dunlop, 2014). The timing of magnetization acquisition relative to independently dated tectonic events can be determined through paleomagnetic fold tests. Additionally, paleomagnetic directions can be compared to temporally calibrated apparent polar wander paths (APWPs), which can provide constraints on absolute chronology. The Negaunee, Goodrich, and intercalated ore bodies are excellent targets for a paired radiometric and paleomagnetic dating approach on specular hematite (specularite) in IF, as they are amenable to paleomagnetic field tests and have an abundance of specularite grains that can be dated via U-Pb LA-ICPMS (Fig. 1; Cannon, 1976). Results from these approaches can be considered in the well-documented tectonomagmatic context of the region. In this study, we develop paired paleomagnetic and *in situ* U-Pb data on hematite-bearing samples to constrain the timing of hematite crystallization both within banded iron formation and enriched hematite iron ore (Fig. 1B). Our combined datasets reveal a previously unrecognized period of hematite mineralization ca. 550 Ma, coinciding with an interval of conspicuous

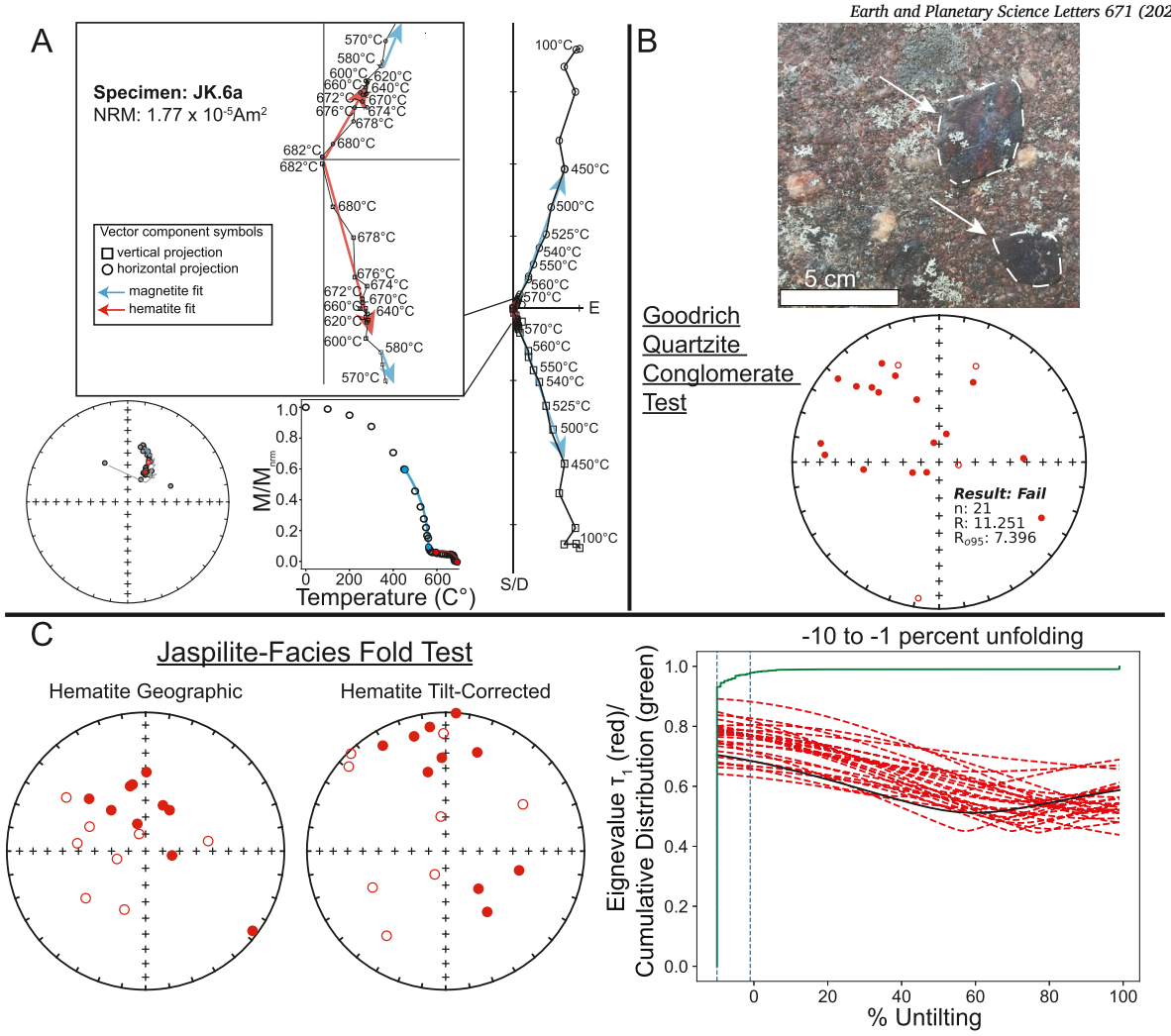

Fig. 2. Paleomagnetic results from the Negaunee Iron Formation and Goodrich Quartzite conglomerate. *(A)* Representative specimen demagnetization data from a jaspilite facies sample (JK.6a) from the top of Jasper Knob (Fig. 1) shown with equal area, natural remnant magnetization (NRM) normalized intensity, and Zijderveld plots. The component unblocking from 450 °C to 580 °C corresponds to remanence held by magnetite (light blue). Inset box is a magnified view of the same Zijderveld diagram to show the origin-trending hematite component that unblocks from 600 °C to 682 °C. *(B)* Results for a conglomerate test conducted on iron formation clasts incorporated within the overlying Goodrich conglomerate at locality GQ5 (Fig. 1A). The dashed white lines and arrows in the photograph highlight sampled iron formation pebbles. The equal area plot shows the hematite paleomagnetic directions, in geographic coordinates, from specimens with interpretable demagnetization behavior. The results of the conglomerate test reveal that R > R_o indicating that the data are distinguishable from random directions at the 95% confidence level and therefore fail a conglomerate test. This result indicates that magnetization was acquired after the iron formation clasts were incorporated into the conglomerate. *C.* Jaspilite facies fold test results for samples taken from the summit of Jasper Knob (JK Top in Fig. 1C). Equal area plots on the left side show that the hematite directions are more dispersed when corrected for tilt. Bootstrap fold test results (Tauxe and Watson, 1994) reveal the tightest cluster of directions (peak of black curve and of red dashed bootstrap resamples summarized by the green CDF curve) to be prior to structural untilting. This result indicates that magnetization was acquired after folding.

tectonic stability in Laurentia's interior. Ancient hematite crystallization decoupled from active tectonism contrasts with the paradigm of orogenesis as the cause of these and other ore deposits.

2. Methods

2.1. Iron formation samples

Three facies with distinct iron oxide textures were targeted for paleomagnetic and geochronologic block sampling. At the top of the Jasper Knob locality (Fig. 1D), the archetypal jaspilite facies IF crops out composed of alternating and tightly folded bands of red polycrystalline quartz (jasper) and grey specular hematite (specularite) with numerous cross-cutting veins and small-scale brecciated zones where jasper is replaced by recrystallized specularite (Fig. 1B). The vibrant red color of the jasper bands stems from dispersed nano-inclusions of <500 nm sized hematite referred to as pigmentary hematite. Coarser grained hematite with grain sizes above > 500 nm is grey with a reflective, metallic luster and is termed specularite (Jiang et al., 2022). Given the distinct orientation of banding associated with folds, this locality enables sampling for a paleomagnetic fold test (Fig. 1). The jaspilite facies was also sampled at the New Richmond mine to the east of Jasper Knob, but was less tightly folded than at Jasper Knob and not included in the fold test. Outcrops on the edge of relict mine pits on the western and southern sides of Jasper Knob exposed a facies enriched in and dominated by specularite (Fig. 1C,S1). This enriched facies has vuggy zones with botryoidal ferric oxides and thinner to absent chert banding that is bleached relative to the vibrant red jasper bands of the jaspilite facies (Figs. 1B,C and S2). The third targeted facies was the basal Goodrich conglomerate, which is composed dominantly of IF clasts in a quartzite matrix (Fig. 2B) that can have interspersed fine-sand-sized martite (hematite pseudomorphed after magnetite) octahedra. The application of a paleomagnetic

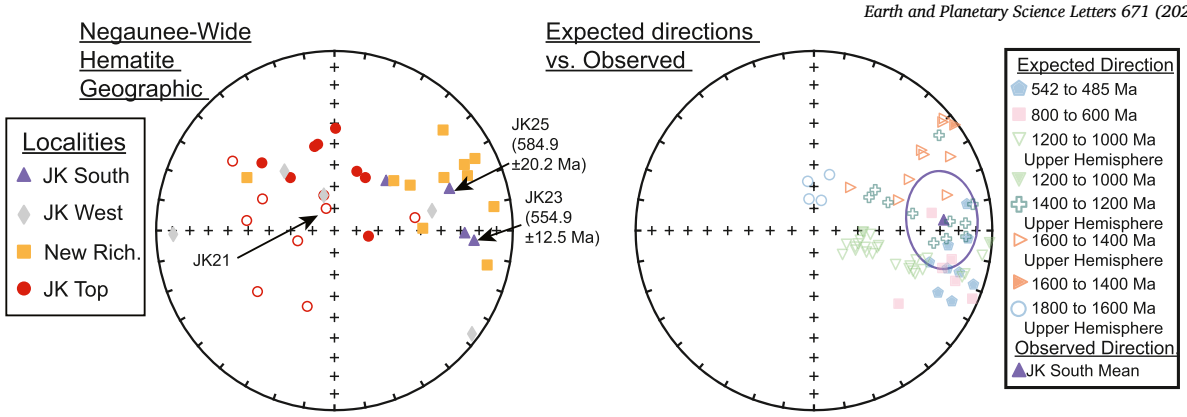

Fig. 3. Directional comparison between observed sites and expected paleomagnetic directions. Equal area plot on the left presents the hematite directions in geographic coordinates for upper Negaunee Iron Formation samples with symbols corresponding to localities. Samples with associated U-Pb dates shown in Fig. 4 are labeled. The equal area plot on the right summarizes expected directions (unified to reversed polarity) for the study area implied from the compiled paleomagnetic poles of refs. (Torsvik et al., 2012; Evans et al., 2021) with symbols binned into 200 Myr intervals. The blue triangle is the Fisher mean with associated α_{95} of the two south Jasper Knob samples with Ediacaran/Cambrian U-Pb dates (JK23 and JK25) grouped with JK22 that has a very similar direction to JK23. This mean direction and associated confidence interval overlaps with the Cambrian directions in agreement with the U-Pb dates.

conglomerate test to IF clasts within the basal Goodrich conglomerate can elucidate the timing of magnetization relative to deposition, providing additional relative chronostratigraphic constraints on hematite grain growth at Jasper Knob. Within the Negaunee Formation, the enriched ore-bearing zone is restricted to the upper jaspilite facies and typically follows the contact with the overlying Goodrich Quartzite (Fig. 1A).

2.2. Paleomagnetic sampling and lab analyses

Oriented paleomagnetic specimen blocks from the sample localities were collected using both a Brunton and sun compass to determine sample surface strike and dip during the 2023 summer field season. The solar azimuth was preferentially used to determine the strike of the paleomagnetic specimens. Structural measurements at each site were measured using the FieldMOVE Clino iPhone application. Sampling of the jaspilite facies at Jasper Knob was focused on collecting specimens that encompassed different dip panels for an informative fold test and sample-specific structural corrections were used during the fold test corresponding to the measured strike and dip of the jaspilite laminations. Clasts of iron formation collected from the Goodrich Quartzite ranged in size from pebbles to cobbles. Paleomagnetic specimens were cut into ~2.5 cm blocks in the University of California (UC) Berkeley rock preparation laboratory using a water cooled rock saw with sister material being preserved to be prepared for LA-ICPMS analyses. Prepared specimens were then subjected to high resolution stepwise thermal demagnetization experiments at the UC Berkeley Paleomagetism Laboratory. An ASC thermal demagnetizer was used to heat the specimens and upon cooling to room temperature in a low field environment (<5 nT) specimens were measured on a 2G DC SQUID Magnetometer. Given the magnetite and hematite remanence, temperature steps were made at progressively higher resolution (down to 2 °C steps) approaching the Curie and Néel temperatures of magnetite and hematite to effectively isolate magnetization. Both hematite and magnetite components were fit using least square lines in specimens with stable demagnetization behavior (Kirschvink, 1980). All paleomagnetic directional data were fit using Pmag GUI and field tests were conducted using the PmagPy Python library (Tauxe et al., 2016) in the Jupyter notebooks located in linked GitHub repository that is also archived on Zenodo. Only data with stable, origin-trending hematite-carrying directions were included within the field tests.

2.3. Geochronology specimen preparation and petrography

Sister specimens from the same oriented blocks prepared for paleomagnetic analyses were cut using a rock saw to fit into 2.5-cm diameter low temperature epoxy mounts. The epoxy-mounted specimens were polished using progressively finer polishing laps up to 0.25 μm grit to ensure a flat and uniform polish. The mounted specimens were inspected with reflected light to characterize different oxide textures and differentiate bright pure hematite grains from martite with relict magnetite or goethitic zones. Grains were characterized via scanning electron microscopy and energy dispersive spectrometry at UC Berkeley to confirm a hematite composition prior to U-Pb analysis.

2.4. Geochronology lab analysis and data reduction

LA-ICPMS U-Pb data were collected at the University of Colorado Boulder in the Thermochronology Research and Instrumentation Laboratory (CU TRaIL), using an ESL 193 nm pulsed excimer laser-ablation system coupled to an Agilent 7900 ICP-MS. Spot locations were carefully selected to avoid inclusions, cracks, and voids. The MR-HFO hematite reference material was used as the primary reference material for the normalization of hematite U-Pb data (Courtney-Davies et al., 2020). The 91500 and RAK-17 zircons, and NIST 610 glass standard were employed as secondary reference materials to evaluate instrument reproducibility (Wiedenbeck et al., 1995; Horstwood et al., 2016; Webb et al., 2020), but not for propagating U-Pb ratio uncertainties. During the analytical sessions, three to four HFO, two zircon, and one NIST standard spots were measured followed by 20 unknown measurements. A spot size of 60 μm was used on the unknown hematite and HFO standard while a spot size of 30 μm or 60 μm was used on the zircon and NIST 610 standards. U-Pb data reduction was completed using the U-Pb geochronology module in Iolite4. In the final data table, we report both the analytical (2σ) standard errors and the propagated standard errors (2σ) that takes into account the reproducibility of the primary standard calibration for each spot (Paton et al., 2010). Given that zircons are not matrix-matched to the hematite unknowns or the MR-HFO primary reference, we do not use them for further external uncertainty propagation (Horstwood et al., 2016). However, the approach of Paton et al. (2010) uses the primary reference standard to iteratively create a pool of 'pseudo-secondary' standards that allows for the estimation of excess analytical uncertainty that can be applied to each spot analysis (i.e. the propagated uncertainty), which is advantageous for measurements on hematite, as there is currently no existing secondary hematite standard. This approach allows us to estimate the analytical uncertainty at each spot while avoiding issues related to the matrix-mismatch between the zircon secondary reference materials and the primary reference material. Following data reduction in Iolite4, we use the spot-mean U-Pb isotope ratios and propagated two standard errors to construct

Tera-Wasserburg plots and isochron fits using the IsoplotR package (Vermeesch, 2018).

3. Results

3.1. Paleomagnetic field tests and directional comparison

Fifty-seven jaspilite and enriched facies paleomagnetic specimens from Jasper Knob and the New Richmond mine (JK and NF sites), in addition to 29 conglomerate specimens from the basal Goodrich (GQ5), were subjected to thermal demagnetization. The paleomagnetic specimens across all three facies exhibited remanent magnetization held by a combination of magnetite and hematite, with an origin-trending component in the majority of samples between the 600 to 690 °C steps that indicates magnetization held by hematite (Fig. 2; Özdemir and Dunlop, 2014). Specularite has been well-documented to have higher unblocking temperatures (>650 °C) than pigmentary hematite, an observation that has been leveraged to distinguish specularite remanence from pigmentary hematite remanence in units with both grain size populations present (Swanson-Hysell et al., 2019b). The origin-trending component of magnetization unblocks sharply approaching the Néel temperature of hematite (~690 °C) indicating that it is held by a population of hematite with sizes >500 nm (i.e. specularite rather than pigmentary hematite Swanson-Hysell et al., 2011, 2019b). These unblocking temperatures are significantly higher than the peak estimated metamorphic temperatures for the sample localities (~ 300 °C; Fig. 1; Haase, 1982; Tohver et al., 2007). The highest metamorphic conditions are recorded in the western portion of the Marquette Syncline region and are interpreted to be associated with a ca. 1.76 Ga metamorphic gneiss dome known as the Republic Node (Fig. 1; Tohver et al., 2007). The localities in this study are from the lower metamorphic grade eastern portion of the region (Fig. 1; Tohver et al., 2007). Given that interpretations of peak metamorphic temperatures are below the unblocking temperature of the specularite, it is likely that magnetization is the result of grain growth (crystallization remanent magnetization; CRM) rather than thermal overprinting (thermal remanent magnetization; TRM). Therefore, the paleomagnetic fold test provides insight into the timing of magnetization relative to Paleoproterozoic deformation and is likely constraining the timing of grain growth. Previous paleomagnetic data developed on the Negaunee jaspilite facies in refs (Symons, 1967a,b) yielded ambiguous fold test results, but used coarse-resolution (six steps) alternating-field demagnetization that is insufficient to isolate remanence held by hematite and did not use least-squared fits to determine the ChRM directions.

The hematite remanent magnetization fails both the fold test conducted on the jaspilite and the conglomerate test on IF clasts within the basal Goodrich Quartzite (Figs. 2B,C, S3, and S4). These results indicate that the hematite magnetizations in both the upper Negaunee and basal Goodrich Quartzite are post-depositional and post-deformational in origin. The large dispersion in paleomagnetic directions in both the basal Goodrich conglomerate and Negaunee Iron Formation jaspilite is consistent with field and petrographic interpretation of multiple generations of hematite development in the form of cross-cutting veins, brecciation, and distinct hematite textures corresponding to multiple populations of iron oxide development. The growth of multiple hematite populations through their magnetic blocking volumes during different episodes would result in a larger spread in the observed directions than would be expected for directions recorded rapidly through more typical processes such as cooling of a lava flow or deposition of a sediment layer. A rapidly deposited or cooled succession of sedimentary or igneous units tend to record continuous snapshots of the geomagnetic field that are less dispersed than the directions observed here, with the dispersion around the mean direction corresponding largely to geomagnetic secular variation. In contrast, the episodic growth of different populations of hematite grains in the Neguanee and Goodrich could have increased dispersion between paleomagnetic sites due to the influence of longer timescale processes (e.g. plate motion). Additionally, the presence of upper and lower hemisphere directions in the jaspilite facies indicates episodic polyphase hematite crystallization across geomagnetic polarity reversals.

The specimens from the jaspilite facies at the New Richmond mine sites (NF9 and NF10) exhibit distinct northeasterly and shallower directions relative to the steeper directions recorded in the jaspilite facies at Jasper Knob. The New Richmond directions are similar to Neoproterozoic directions published for the ca. 990 Ma Jacobsville Formation (Zhang et al., 2024), but attempts to date specimens from the jaspilite facies at New Richmond yielded insufficient spread in uranium concentration to assign an age to these directions.

The hematite-carrying remanence component directions of the enriched facies specimens from the south and west mined pits at Jasper Knob exhibit considerable paleomagnetic directional dispersion between the two pits, which suggests a complex and polyphase development of different hematite populations (Fig. 3). The two paleomagnetic samples with Ediacaran and Cambrian U-Pb dates (discussed below, JK23 and JK25), and a co-located sample with a similar direction (JK22), from the southern mine pit yielded a Fisher mean declination/inclination of 085.3°/27.8° with an α_{95} of 19° (Figs. 3 and 4). This mean direction encompasses the expected Cambrian directions for the field site inferred from compiled paleomagnetic poles for Laurentia (Fig. 3; Torsvik et al., 2012).

3.2. Hematite U-Pb geochronology

Five samples from Jasper Knob and the New Richmond Mine yielded interpretable U-Pb dates: one specimen (GQ6-2) is from the basal Goodrich Quartzite near the inferred lower contact, one is from the jaspilite facies (JK21) of the Negaunee Iron Formation, and three specimens are from the enriched facies (JK23, JK25, and Fe Grab) of the Negaunee Iron Formation (Fig. 4). The >100 μm martite grains within GQ6-2 have very low uranium concentrations and could not be dated. The fiborous microplaty hematite texture that fills the interstices between the quartz and martite grains yielded a lower intercept date of 1551.1 ± 82.4 Ma (2σ analytical uncertainty; Fig. 4), which is younger than the depositional age of the conglomerate which is constrained between 1874 and 1850 Ma (Fig. 1).

Most jaspilite facies specimens proved difficult to date due to low uranium concentration and restricted compositional spread, particularly in the coarse hematite veins. However, sample JK21 has sufficient variation in radiogenic uranium concentrations to yield an interpretable Tera-Wasserburg lower intercept date of 1236.4 ± 86.0 Ma on martite grains within the bands of the jaspilite texture (2 σ uncertainty; Fig. S5). A coarse specularite vein that cross-cuts the jaspilite bands was also dated from JK21 and yielded a 1016.2 ± 120.1 Ma but had very low uranium concentration, with points plotting far from concordia (Fig. S5). Even with the very low uranium concentration, the vein data points show a shallower trajectory than the bands when plotted together and the younger age is consistent with the cross-cutting relationship between the vein and jaspilite bands. Although imprecise, the vein date overlaps with the time interval of Midcontinent Rift magmatic activity (Fig. 4). Regionally, the Marquette-Baraga mafic dikes and the ca. 1107 Ma mafic-ultramafic Eagle intrusive complex intruded into the Marquette Range Supergroup (Ding et al., 2010). Fluid migration associated with this magmatism may have contributed to an episode of jaspilite hematite crystallization, but the lack of sufficient compositional spread in Tera-Wasserburg space makes it difficult to confidently associate the vein with rift magmatism.

The three enriched facies samples of the Negaunee Iron Formation from the Jasper Knob southern mine pit and New Richmond Mine yielded much younger dates of 584.9 ± 20.2 Ma (JK25), 554.9 ± 12.9 Ma (JK23), and 467.2 ± 24.7 Ma (Fe Grab). In sample JK25, the martite grains are subhedral and form a more massive, interlocking, texture than in the other facies. In many regions, the grain boundaries between individual crystals are not visible, in contrast to the distinct

grain boundaries in GQ6-2. Sample JK23 has an age with uncertainties that straddle the Ediacaran-Cambrian boundary and is porous with botryoidal ferric oxides infilling the void space that is evident in hand sample and backscatter electron imagery (Fig. 4). The more massive texture and increased porosity is consistent with volume loss due to coupled dissolution-reprecipitation during interactions with fluids as observed in similar hematite ore deposits in the Gogebic Iron Range, MI (Farley and McKeon, 2015; Zhao et al., 2019, (Fig. 4, S2)). The enriched facies specimen from the New Richmond Mine (Fe Grab) is dominated by tightly intergrown and porous martite and gave the youngest Tera-Wasserburg lower intercept date. The age of Fe Grab overlaps with the early portion of the Tippecanoe Transgression which is one of the early Paleozoic epicontinental flooding events recorded on Laurentia (Tasistro-Hart and Macdonald, 2023). The three youngest dated samples exhibit concentrations of uranium that are higher than the other lithofacies. These U concentration indicate that these hematite bodies crystallized from a fluid source distinct from the studied hematite in the jaspilite and basal Goodrich. Furthermore, the resulting spread in $^{238}U/^{206}Pb$ values and higher radiogenic to common Pb ratios make it so that these 584.9 ± 20.2 Ma, 554.9 ± 12.9 Ma, and 467.2 ± 24.7 Ma dates are the most precise in this study.

These results are consistent with episodic hematite growth in ore bodies decoupled from active tectonics rather than enrichment driven only by fluxes of deeply sourced metamorphic or hydrothermal fluids linked to orogenic events as has been argued elsewhere (Pietrzak-Renaud and Davis, 2014; Rasmussen et al., 2016). The multiple observed ages associated with different hematite textures from a narrow geographic area is emblematic of a progressive evolution of IF-hosted ore and highlights the need to consider the age of the hematite itself rather than metamorphic chronometers alone that may not be genetically related to the host oxide textures (Courtney-Davies et al., 2022).

4. Discussion

4.1. Ore formation during tectonic quiescence

The duration of ore crystallization captured by the three ore samples (ca. 580 to 440 Ma) coincides with a period of extended tectonic stability in the interior of Laurentia (cratonic North America). Neoproterozoic to Paleozoic stability contrasts with the numerous regional tectonomagmatic events of the preceding Paleoproterozoic and Mesoproterozoic eras (Fig. 5). The Marquette Range Supergroup (MRS), including the Goodrich and Negaunee Formations, was deposited into a tectonically active arc-related basin ca. 1880 Ma and was subsequently deformed during a sequence of Paleoproterozoic accretionary orogenic events (Schulz and Cannon, 2007). Emplacement of the Humboldt granite ca. 1805 (Holm et al., 2005) was followed by granite-cored gneiss dome collapse between ca. 1800 and 1730 Ma (Tohver et al., 2007), resulting in metamorphism including monazite growth as documented by ref. (Rasmussen et al., 2016) (Fig. 1). Latest Paleoproterozoic to earliest Mesoproterozoic metamorphism at the time of the Mazatzal orogeny is recorded farther to the south by ca. 1615 to 1575 Ma mica ^{40}Ar-^{39}Ar dates (Holm et al., 2019). The Baraboo orogeny followed with associated emplacement of the ca. 1470 Ma Wolf River batholith and is the last major orogenic event in this region (Dewane and Van Schmus, 2007; Medaris et al., 2021; Swanson-Hysell, 2021). The large uncertainty on the 1551.1 ± 82.4 Ma date from the fibrous microplaty hematite in the basal Goodrich overlaps with both the Mazatzal orogeny and Wolf River Batholith emplacement, making it difficult to implicate either event as the driver of hematite crystallization in this sample. This date is close to, but does not overlap within uncertainty, the youngest xenotime date of 1660 ± 56 from the basal Goodrich (Rasmussen et al., 2016).

The Marquette syncline was on the margin of the Midcontinent Rift which was associated with lithospheric extension and voluminous volcanism from ca. 1109 to 1083 Ma (Cannon, 1994; Swanson-Hysell et al., 2019a). The ca. 1107 Ma Eagle mafic-ultramafic intrusive complex and associated Marquette Baraga dikes were emplaced into the Marquette Range Supergroup during the early stage of Midcontinent Rift magmatism (Ding et al., 2010). This timing is indistinguishable from the 1016.2 ± 120.1 Ma date from the jaspilite facies vein (JK21), and the emplacement of the Baraga dikes could have generated hydrothermal fluids to drive a later stage of jaspilite mineralization following ca. 1800 to 1500 Ma hypogene enrichment indicated by the hematite and accessory mineral dates (Fig. 5). The termination of the Midcontinent Rift is linked to far-field compressional stress from the Grenville orogeny on the eastern margin of Laurentia associated with the assembly of Rodinia (Swanson-Hysell et al., 2023). The Grenvillian orogeny caused minor contractional deformation in the Marquette Range Supergroup and small-scale syn-orogenic basin development near the end of the orogeny ca. 980 Ma, culminating in long-term tectonic stability of the region within the continental interior (Hodgin et al., 2022; Alemu et al., 2023; Hodgin et al., 2024).

Following an interval of supercontinent stability from ca. 980 to 780 Ma, rifting initiated along the western, eastern, and southern margins of Laurentia (Macdonald et al., 2023). This rifting was associated with the breakup of Rodinia and occurred diachronously along the margins from ca. 780 to 530 Ma (Swanson-Hysell, 2021; Macdonald et al., 2023). The farthest extent of eastern margin volcanism in this region is the ca. 585 Ma Grenville Dikes occurring >450 km to the east of our field locality (Halls et al., 2015). The ca. 585-465 Ma U-Pb age constraints on the hematite and the location of the field site in the stable interior, far away from rifting along Laurentia's margins, indicates that the development of the enriched hematite ore bodies was decoupled from either the assembly or breakup of Rodinia.

To the south and east of the field area, the flat-lying Cambrian sandstone of the Munising Formation caps an angular unconformity with the underlying Archean, Paleoproterozoic, and Neoproterozoic units (Fig. 1). The Munising was deposited associated with the Sauk Transgression (Haddox and Dott, 1990). The Sauk Transgression is an interval of continental flooding that resulted in the widespread deposition of Cambrian marine strata across Laurentia (Runkel et al., 2012; Karlstrom et al., 2018; Tasistro-Hart and Macdonald, 2023). Early Paleozoic Laurentia also experienced several other intervals of epicontinental flooding including the ca. 460 Ma Tippecanoe Transgression that deposited Ordovician marine sequences to the south and east of the field region (Smith et al., 1996; Tasistro-Hart and Macdonald, 2023). The Munising Formation extends to within 30 km of Jasper Knob in the present-day. It likely overlaid Marquette Range Supergroup strata in the field area at the time of deposition. This inference is consistent with observations of Munising in direct contact with similar aged strata to the east and south (Hamblin, 1958) including it unconformably overlying the Negaunee-correlative Vulcan Iron Formation to the south (Cumberlidge and Stone, 1964). The presence of an angular unconformity between the nearly flat-lying shallow marine sandstone of the Munising Formation and Archean and Paleoproterozoic units to the ~30 km to south of Jasper Knob at a similar elevation indicates that at the time of ore formation the Negaunee and Goodrich lithologies were situated in the near-surface.

(U-Th)/^{21}Ne dates developed from cm to decimeter scale hematite crystals from the Gogebic hematite ore from the Ashland and Pabst mines, 200 km to the southwest of Jasper Knob were interpreted to indicate hematite crystallization at 789 ± 48 Ma, 756 ± 18 Ma, and 453 ± 14 Ma (Farley and McKeon, 2015, Fig. 4). These data provide additional evidence of hematite crystallization during the interval of tectonic stability in Laurentia's interior. Additionally, $^{4}He/^{3}He$ thermochronometry on these hematite crystals indicate that their precipitation occurred at 150 ±70 °C at 770 Ma and ~60 °C at 450 Ma consistent with burial in the relatively near surface depending on interpreted geothermal gradient (Farley and McKeon, 2015; Hodgin et al., 2024). Thermal history modeling incorporating basement zircon and apatite (U-Th)/He dates 250 km to the north in the southern Canadian Shield suggests the latest possible cooling below 100 °C (~2 km with a 30°/km geotherm and a

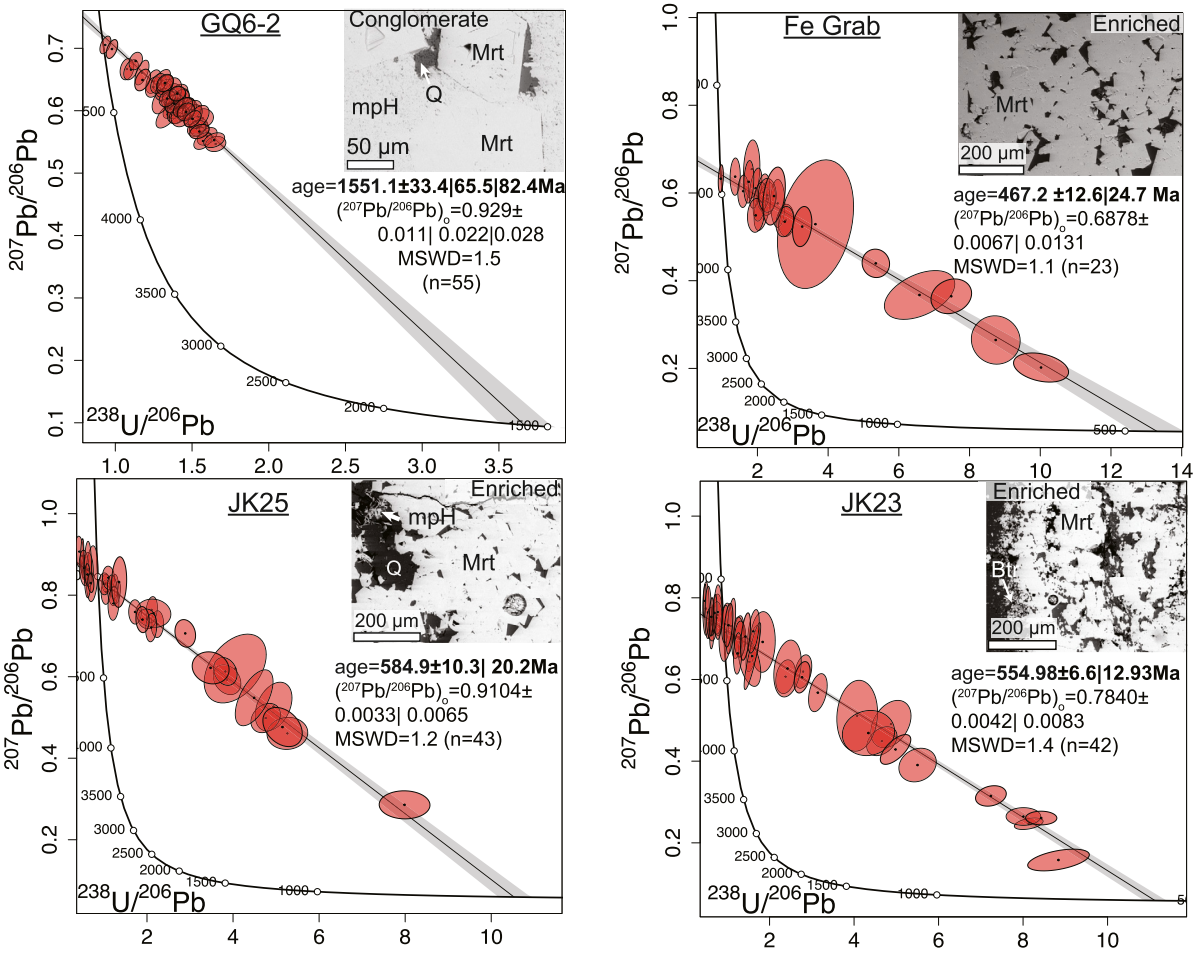

Fig. 4. Hematite U-Pb geochronology results. *(A)* Tera-Wasserburg discordia plots for samples from the basal Goodrich (GQ6-2) and enriched-facies (Fe Grab, JK23 and JK25) at the New Richmond Mine and Jasper Knob. The ellipses are the individual analyses and are plotted with their internal propagated standard errors (2σ), which include uncertainties associated with the downhole fraction correction and the reproducibility of the primary hematite standard through the measurement sessions (Paton et al., 2010; Vermeesch, 2018). Lower intercept ages for each specimen are reported with 2σ analytical uncertainties and are inset within the respective plots. Inset in the upper right corner of each plot are backscatter electron (BSE) images of each sample showing hematite textures. In GQ6-2, the fibrous microplaty hematite (mph) yielded the data shown in the Tera-Wasserburg plot while the euhedral martite (Mrt) in the darker quartz (Q) matrix was too low in uranium to yield an interpretable date. The martite textures yielded the data in the plots for Fe Grab, JK23 and JK25. Intergrown botryoidal ferric oxides (Btr) fills much of the void space.

surface temperature of 30°) occurred between ca. 650 to 450 Ma (Peak et al., 2023; Sturrock et al., 2024). These interpreted thermal histories indicate that the Negaunnee-Goodrich contact was positioned at shallow burial depths during hematite ore crystallization.

There are several independent lines of evidence to support the interpretation that the dates are primary crystallization ages and have not subsequently been reset. The paleomagnetic data on the enriched facies do not show evidence of secondary thermal overprints, in particular there are no clear major directional deflections in the lower to middle temperature demagnetization steps (300 to 500 °C). Magnetization components unblocking in this temperature range are the least stable and would be the most susceptible to thermal overprints. The regional tectonothermal constraints from the metamorphic thermometers and the previously described thermochronology also supports that the field localities have not experienced prolonged thermal perturbations greater than 300 °C since the Paleoproterozoic. The closure temperature of the U-Pb system in hematite has not been evaluated via diffusion experiments, but existing geochronologic information from other dated hematite deposits provides compelling evidence that the closure temperature of hematite is sufficiently high enough to not have been reset in our study region and a reliable geochronometer within similar age strata (Keyser et al., 2019; Courtney-Davies et al., 2024). Previous work on hematite in iron ore using U-Pb ID-TIMS has yielded concordant hematite ages that agree with other geochronologic constraints from the same deposit, whereas populations of xenotime from the same site have been reset (Cherry et al., 2018; Courtney-Davies et al., 2019). While magnetite and hematite likely have different Pb closure temperatures, insights from recent Pb diffusion experiments in magnetite indicate a U-Pb closure temperature of ~550 °C (Watson et al., 2023). Hematite likely has a similarly high U-Pb closure temperature given the previously described circumstantial evidence that has shown hematite to be a recalcitrant geochronometer. Furthermore, there is no evidence for late Neoproterozoic and early Paleozoic tectonothermal activity in interior Laurentia, which represents a uniquely long period of stasis in the continent's history (Swanson-Hysell, 2021).

The age of hematite ore crystallization at Jasper Knob and New Richmond spans an interval of ca. 100 Ma that is consistent with protracted iron enrichment driven by warm meteoric waters mobilized downward along faults or fractures to the shallow subsurface rather than subaerial lateritic oxidation. Weathering-driven enrichment is apparent in many

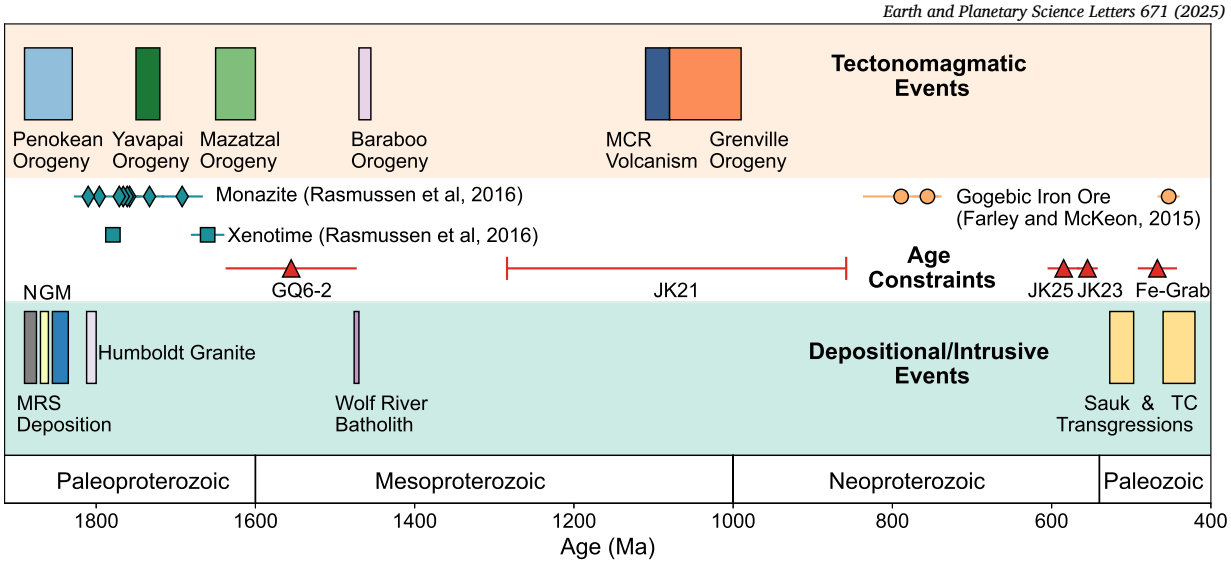

Fig. 5. Timeline of regional tectonic events in relation to iron formation geochronology. *Upper panel:* The major tectonomagmatic events that influenced the region are shown as colored rectangles with the width of each block corresponding to their interpreted duration (Swanson-Hysell, 2021; Holm et al., 2020; Zi et al., 2022). *Lower panel:* The depositional and intrusive events corresponding to relevant regional units (Schneider et al., 2002; Tohver et al., 2007; Pietrzak-Renaud and Davis, 2014; Dewane and Van Schmus, 2007). Each formation within the Marquette Range Supergroup is denoted by the letters above each block (N: Negaunee; G: Goodrich; M: Michigamme). The *middle* panel presents U-Pb dates (with 2σ uncertainties) from monazite and xenotime (blue diamond and squares respectively) from the Negaunee, Goodrich, and hematitic ore bodies (Rasmussen et al., 2016). (U-Th)/^{21}Ne dates from cm-scale hematite crystals associated with Gogebic iron range ore near Ironwood, MI are plotted as orange circles (Farley and McKeon, 2015). Hematite U-Pb dates from this study (Fig. 4) are shown as red triangles. JK21 is from the jaspilite facies at Jasper Knob and yielded two dates from two distinct textures (Fig. S5). Due to the age complexity associated with this sample, we present these data as a dashed bracket that spans the 2σ uncertainty of both the martite and vein textures that represents a large time window for hematite enrichment.

IF-hosted ore deposits but has been associated with the development of soft, massive, goethitic ore in the late Mesozoic and Cenozoic related to lateritic weathering in a hothouse climate, whereas our U-Pb and paleomagnetic data indicate that the enriched hematite facies significantly predates this interval and the ore at Jasper Knob and New Richmond has not been subjected to texturally obliterating surficial weathering (Spier et al., 2006; Lascelles, 2012; Thorne et al., 2014; Angerer et al., 2021). The shallow paleomagnetic inclinations on samples JK22, JK23, and JK25 indicate that the hematite within the enriched facies acquired their remanance during crystallization at tropical latitudes (~14°) in the late Ediacaran and early Paleozoic when surface temperatures have been estimated to be significantly higher than those today (35-40 °C) (Wotte et al., 2019; Bergmann et al., 2025). Regional faults could have served as a conduit for warm, weakly acidic, fluids to permeate downward into the subsurface where they facilitated dissolution of jasper and Fe^{2+} bearing phases (magnetite), leading to the increased porosity observed in the enriched facies and the reprecipitation of hematite through a combination of redox-independent and redox dependent processes, as has been observed experimentally (Ohmoto, 2003; Otake et al., 2010; Zhao et al., 2019).

There remains significant debate regarding the original mineralogical composition of IF, specifically whether ferric oxyhydroxides (e.g. ferrihydrite) or reduced iron silicates (e.g. greenalite) were the primary iron-bearing phases at the time of deposition (Konhauser et al., 2017; Robbins et al., 2019; Rasmussen et al., 2021). This debate is of critical importance to geochemical interpretations of the oxidation state of ancient marine systems. However, as demonstrated in this study, the prolonged polygenetic history of hematite formation in many IF facies complicates direct assessments of original mineralogy. Hematite ore development and enrichment of the host-IF occurs through distinct sets of processes from those that occurred during the diagenesis of the IF protolith. An often-overlooked complexity in the study of IF is the prolonged history of iron oxide development characterized by profound recrystallization that obscures the original mineral assemblage (Hagemann et al., 2016). Efforts aimed at constraining original IF mineralogy, or seeking to apply IF geochemistry to gain insight into ancient environments, must recognize that recrystallization can be pervasive and multi-stage. Such processes can profoundly obscure primary depositional characteristics, particularly in proximity to ore bodies, as we have demonstrated in this work and is observed in other ore districts (Angerer et al., 2021).

5. Conclusion

Our paired dataset reveals that hematite ore development has greater nuance and spans a broader duration then previously recognized from dating metamorphic chronometers alone. Across all sampled facies, the paleomagnetic and U-Pb data yielded mutually compatible interpretations of hematite crystallization and indicate that ore formation was not driven purely by tectonic processes. A major stage of ore formation in this region occurred in the Ediacaran and early Phanerozoic during a protracted interval of stability across Laurentia associated with the transgression of warm, tropical epicontinental seaways. This insight would not be discernible in the absence of direct ages on the hematite and cautions against ascribing hematite growth to discrete tectonic events in the geologic record.

CRediT authorship contribution statement

Anthony J. Fuentes: Writing – review & editing, Writing – original draft, Visualization, Methodology, Investigation, Funding acquisition, Formal analysis, Data curation, Conceptualization. **Liam Courtney-Davies:** Writing – review & editing, Visualization, Formal analysis, Data curation. **Rebecca Flowers:** Writing – review & editing, Funding acquisition. **Yiming Zhang:** Writing – review & editing, Investigation. **Nicholas Swanson-Hysell:** Writing – review & editing, Supervision, Methodology, Funding acquisition, Conceptualization.

Declaration of competing interest

The authors declare that they have no known competing financial interests or personal relationships that could have appeared to influence the work reported in this paper.

Acknowledgements

Research support for the project was provided by NSF EAGER grant EAR-2203547 to N.L.S-H. and EAR-2203532 to R.M.F., NSF Instrumentation and Facilities grant EAR-1920648 to R.M.F., a Future Investigator in NASA Earth and Space Science and Technology (FINNEST) award 80NSSC22K1369 and a Ford Foundation Predoctoral Fellowship to A.J.F. We thank Peter Martin for initiating this collaborative research trajectory during his time as a postdoc at CU. We thank John Grimsich for assistance with sample preparation and SEM/EDS characterization. We thank Bill Cannon for his insights on the local geology that were valuable in identifying field sampling localities. We acknowledge the help of Michael Kouyoumdjian with literature review. We thank Andrew Kylander-Clark and Kurt Konhauser for their thoughtful reviews that greatly improved the manuscript.

Appendix A. Supplementary material

Supplementary material related to this article can be found online at https://doi.org/10.1016/j.epsl.2025.119621.

Data availability

All datasets and code used for analyses are available in the study GitHub repository (https://github.com/Swanson-Hysell-Group/Negaunee_Goodrich). The paleomagnetic data for this study are available in the MaGIC database (https://doi.org/10.7288/V4/MAGIC/20184. All code and data are also archived on Zenodo (https://doi.org/10.5281/zenodo.13883216).

References

Alemu, T.B., Hodgin, E.B., Swanson-Hysell, N.L., 2023. Grooving in the midcontinent: a tectonic origin for the mysterious striations of L'Anse Bay, Michigan, USA. Geosphere 19, 1291–1299.

Angerer, T., Hagemann, S.G., Walde, D.H., 2021. Diagenetic and supergene ore forming processes in the iron formation of the Neoproterozoic Jacadigo Group, Corumbá, Brazil. J. S. Am. Earth Sci. 105, 102902.

Angerer, T., Thorne, W., Hagemann, S.G., Tribus, M., Evans, N.J., Savard, D., 2022. Iron oxide chemistry supports a multistage hydrothermal genesis of BIF-hosted hematite ore in the Mt. Tom Price and Mt. Whaleback deposits. Ore Geol. Rev. 144, 104840.

Bergmann, K.D., Macdonald, F.A., Swanson-Hysell, N.L., 2025. The causes and consequences of ordovician cooling. Annu. Rev. Earth Planet. Sci. 53, 651–685. https://doi.org/10.1146/annurev-earth-040523-114630.

Cannon, W.F., 1976. Hard iron ore of the Marquette Range, Michigan. Econ. Geol. 71, 1012–1028. https://doi.org/10.2113/gsecongeo.71.6.1012.

Cannon, W.F., 1994. Closing of the Midcontinent rift-A far—field effect of Grenvillian compression. Geology 22, 155–158.

Cannon, W.F., Klasner, J.S., 1976. Geological map and geophysical interpretation of the Witch Lake Quadrangle, Marquette, Iron, and Baraga Counties, Michigan. Report. US Geological Survey. https://pubs.usgs.gov/publication/i987.

Cannon, W.F., Klasner, J.S., 1977. Bedrock geologic map of the southern part of the Diorite and Champion 7 1/2 minute quadrangles, Marquette County, Michigan. Report. US Geological Survey, Reston, VA.

Cherry, A., Kamenetsky, V., McPhie, J., Thompson, J., Ehrig, K., Meffre, S., Kamenetsky, M., Krneta, S., 2018. Tectonothermal events in the Olympic IOCG Province constrained by apatite and REE-phosphate geochronology. Aust. J. Earth Sci. 65, 643–659.

Courtney-Davies, L., Danišik, M., Ramanaidou, E.R., Kirkland, C.L., Evans, N.J., Piechocka, A.M., McInnes, B.I., 2022. Hematite geochronology reveals a tectonic trigger for iron ore mineralization during Nuna breakup. Geology 50, 1318–1323.

Courtney-Davies, L., Fiorentini, M., Dalstra, H., Hagemann, S., Ramanaidou, E., Danišik, M., Evans, N.J., Rankenburg, K., McInnes, B.I., 2024. A billion-year shift in the formation of Earth's largest ore deposits. Proc. Natl. Acad. Sci. USA 121, e2405741121.

Courtney-Davies, L., Gilbert, S.E., Ciobanu, C.L., Tapster, S.R., Richardson, M.W., Cook, N.J., Wade, B.P., Verdugo-Ihl, M.R., Ehrig, K., Condon, D.J., 2020. A synthetic haematite reference material for LA-ICP-MS U-Pb geochronology and application to iron oxide-Cu-Au systems. Geostand. Geoanal. Res. 45, 143–159. https://doi.org/10.1111/ggr.12365.

Courtney-Davies, L., Tapster, S.R., Ciobanu, C.L., Cook, N.J., Verdugo-Ihl, M.R., Ehrig, K.J., Kennedy, A.K., Gilbert, S.E., Condon, D.J., Wade, B.P., 2019. A multi-technique evaluation of hydrothermal hematite UPb isotope systematics: implications for ore deposit geochronology. Chem. Geol. 513, 54–72.

Cumberlidge, J.T., Stone, J.G., 1964. The vulcan iron formation at the Groveland Mine, Iron Mountain, Michigan. Econ. Geol. 59, 1094–1106.

Davis, D.W., 2008. Sub-million-year age resolution of Precambrian igneous events by thermal extraction–thermal ionization mass spectrometer Pb dating of zircon: application to crystallization of the Sudbury impact melt sheet. Geology 36, 383–386.

Dewane, T., Van Schmus, W., 2007. U–Pb geochronology of the Wolf River batholith, North-central Wisconsin: evidence for successive magmatism between 1484 Ma and 1468 Ma. Precambrian Res. 157, 215–234.

Ding, X., Li, C., Ripley, E.M., Rossell, D., Kamo, S., 2010. The Eagle and East Eagle sulfide ore-bearing mafic-ultramafic intrusions in the Midcontinent Rift System, upper Michigan: geochronology and petrologic evolution. Geochem. Geophys. Geosyst. 11. https://doi.org/10.1029/2009gc002546.

Dukino, R., England, B., Kneeshaw, M., 2000. Phosphorus distribution in BIF-derived iron ores of Hamersley province, western Australia. Appl. Earth Sci. 109, 168–176.

Evans, D.A.D., Pesonen, L.J., Eglington, B.M., Elming, S.Å, Gong, Z., Li, Z.X., McCausland, P., Meert, J., Mertanen, S., Pisarevsky, S., Pivarunas, A., Salminen, J., Swanson-Hysell, N., Torsvik, T., Trindade, R., Veikkolainen, T., Zhang, S., 2021. An expanding list of reliable paleomagnetic poles for Precambrian tectonic reconstructions. In: Pesonen, L.J., Evans, D.A.D., Elming, S.Å, Salminen, J.M., Veikkolainen, T. (Eds.), Ancient Supercontinents and the Paleogeography of the Earth. Elsevier, pp. 605–639.

Evans, K., McCuaig, T., Leach, D., Angerer, T., Hagemann, S.G., 2013. Banded iron formation to iron ore: a record of the evolution of Earth environments? Geology 41, 99–102.

Farley, K.A., McKeon, R., 2015. Radiometric dating and temperature history of banded iron formation–associated hematite, Gogebic iron range, Michigan, USA. Geology.

Gair, J.E., Han, T.M., 1975. Bedrock geology and ore deposits of the Palmer Quadrangle, Marquette County, Michigan, with a section on the Empire Mine. Technical Report. US Geological Survey.

Haase, C.S., 1982. Metamorphic petrology of the Negaunee Iron Formation, Marquette District, northern Michigan; mineralogy, metamorphic reactions, and phase equilibria. Econ. Geol. 77, 60–81.

Haddox, C.A., Dott, R.H., 1990. Cambrian shoreline deposits in northern Michigan. J. Sediment. Res. 60, 697–716.

Hagemann, S., Rosière, C., Lobato, L., Baars, F., Zucchetti, M., Figueiredo e Silva, R., 2006. Controversy in genetic models for proterozoic high-grade, banded iron formation (BIF)-related iron deposits–unifying or discrete model (s)? Appl. Earth Sci. 115, 147–151.

Hagemann, S.G., Angerer, T., Duuring, P., Rosière, C.A., e Silva, R.F., Lobato, L., Hensler, A., Walde, D., 2016. BIF-hosted iron mineral system: a review. Ore Geol. Rev. 76, 317–359.

Halls, H.C., Lovette, A., Hamilton, M., Söderlund, U., 2015. A paleomagnetic and U–Pb geochronology study of the western end of the Grenville dyke swarm: rapid changes in paleomagnetic field direction at ca. 585 Ma related to polarity reversals? Precambrian Res. 257, 137–166.

Hamblin, W.K., 1958. The Cambrian Sandstones of Northern Michigan. University of Michigan.

Hodgin, E.B., Swanson-Hysell, N.L., DeGraff, J.M., Kylander-Clark, A.R., Schmitz, M.D., Turner, A.C., Zhang, Y., Stolper, D.A., 2022. Final inversion of the midcontinent rift during the rigolet phase of the Grenvillian orogeny. Geology 50, 547–551.

Hodgin, E.B., Swanson-Hysell, N.L., Kylander-Clark, A.R., Turner, A.C., Stolper, D.A., Ibarra, D.E., Schmitz, M.D., Zhang, Y., Fairchild, L.M., Fuentes, A.J., 2024. One billion years of stability in the North American Midcontinent following two-stage Grenvillian structural inversion. Tectonics 43, e2024TC008415.

Holm, D., Medaris Jr, L.G., McDannell, K.T., Schneider, D.A., Schulz, K., Singer, B.S., Jicha, B.R., 2020. Growth, overprinting, and stabilization of Proterozoic provinces in the southern Lake Superior region. Precambrian Res. 339, 105587.

Holm, D.K., Gordon Medaris, L., McDannell, K.T., Schneider, D.A., Schulz, K., Singer, B.S., Jicha, B.R., 2019. Growth, overprinting, and stabilization of Proterozoic Provinces in the southern Lake Superior region. Precambrian Res. https://doi.org/10.1016/j.precamres.2019.105587.

Holm, D.K., Van Schmus, W.R., MacNeill, L.C., Boerboom, T.J., Schweitzer, D., Schneider, D., 2005. U-Pb zircon geochronology of paleoproterozoic plutons from the northern midcontinent, USA: evidence for subduction flip and continued convergence after geon 18 Penokean orogenesis. Geol. Soc. Am. Bull. 117, 259–275.

Horstwood, M.S., Košler, J., Gehrels, G., Jackson, S.E., McLean, N.M., Paton, C., Pearson, N.J., Sircombe, K., Sylvester, P., Vermeesch, P., et al., 2016. Community-derived standards for LA-ICP-MS U-(Th-) Pb geochronology–Uncertainty propagation, age interpretation and data reporting. Geostand. Geoanal. Res. 40, 311–332.

Jiang, Z., Liu, Q., Roberts, A.P., Dekkers, M.J., Barrón, V., Torrent, J., Li, S., 2022. The magnetic and color reflectance properties of hematite: from Earth to Mars. Rev. Geophys. 60. https://doi.org/10.1029/2020rg000698.

Karlstrom, K., Hagadorn, J., Gehrels, G., Matthews, W., Schmitz, M., Madronich, L., Mulder, J., Pecha, M., Giesler, D., Crossey, L., 2018. Cambrian Sauk transgression in the Grand Canyon region redefined by detrital zircons. Nat. Geosci. 11, 438–443.

Keyser, W., Ciobanu, C.L., Cook, N.J., Dmitrijeva, M., Courtney-Davies, L., Feltus, H., Gilbert, S., Johnson, G., Ehrig, K., 2019. Iron-oxides constrain BIF evolution in terranes with protracted geological histories: the iron count prospect, Middleback ranges, south Australia. Lithos 324, 20–38.

Kirschvink, J., 1980. The least-squares line and plane and the analysis of palaeomagnetic data. Geophys. J. Int. 62, 699–718.

Konhauser, K.O., Planavsky, N., Hardisty, D., Robbins, L., Warchola, T., Haugaard, R., Lalonde, S., Partin, C., Oonk, P., Tsikos, H., et al., 2017. Iron formations: a global record of Neoarchaean to Palaeoproterozoic environmental history. Earth-Sci. Rev. 172, 140–177.

Lascelles, D., 2012. Banded iron formation to high-grade iron ore: a critical review of supergene enrichment models. Aust. J. Earth Sci. 59, 1105–1125.

Macdonald, F.A., Yonkee, W.A., Flowers, R.M., Swanson-Hysell, N.L., 2023. Neoproterozoic of Laurentia. In: Laurentia: Turning Points in the Evolution of a Continent. Geological Society of America.

Medaris Jr, L.G., Singer, B.S., Jicha, B.R., Malone, D.H., Schwartz, J.J., Stewart, E.K., Van Lankvelt, A., Williams, M.L., Reiners, P.W., 2021. Early mesoproterozoic evolution of midcontinental Laurentia: defining the geon 14 Baraboo orogeny. Geosci. Front. 12, 101174.

Morris, R., Wolff, K., 1985. Genesis of iron ore in banded iron-formation by supergene and supergene-metamorphic processes—a conceptual model. In: Handbook of Strata-Bound and Stratiform Ore Deposits, vol. 13, pp. 73–235.

Ohmoto, H., 2003. Nonredox transformations of magnetite-hematite in hydrothermal systems. Econ. Geol. 98, 157–161.

Otake, T., Wesolowski, D.J., Anovitz, L.M., Allard, L.F., Ohmoto, H., 2010. Mechanisms of iron oxide transformations in hydrothermal systems. Geochim. Cosmochim. Acta 74, 6141–6156.

Özdemir, Ö., Dunlop, D.J., 2014. Hysteresis and coercivity of hematite. J. Geophys. Res., Solid Earth 119, 2582–2594.

Paton, C., Woodhead, J.D., Hellstrom, J.C., Hergt, J.M., Greig, A., Maas, R., 2010. Improved laser ablation U-Pb zircon geochronology through robust downhole fractionation correction. Geochem. Geophys. Geosyst. 11. https://doi.org/10.1029/2009gc002618.

Peak, B.A., Flowers, R.M., Macdonald, F.A., 2023. Ediacaran-Ordovician tectonic and geodynamic drivers of great unconformity exhumation on the southern Canadian shield. Earth Planet. Sci. Lett. 619, 118334.

Pietrzak-Renaud, N., Davis, D., 2014. U–Pb geochronology of baddeleyite from the Belleview metadiabase: age and geotectonic implications for the Negaunee Iron Formation, Michigan. Precambrian Res. 250, 1–5.

Powell, C.M., Oliver, N.H., Li, Z.X., Martin, D.M., Ronaszeki, J., 1999. Synorogenic hydrothermal origin for giant Hamersley iron oxide ore bodies. Geology 27, 175–178.

Puffett, W.P., 1974. Geology of the Negaunee Quadrangle, Marquette County, Michigan. Technical Report. US Government Printing Office.

Ramanaidou, E.R., Morris, R., 2010. Comparison of supergene mimetic and supergene lateritic iron ore deposits. Appl. Earth Sci. 119, 35–39. https://doi.org/10.1179/037174510X12853354810589.

Rasmussen, B., Fletcher, I.R., Muhling, J.R., Thorne, W.S., Broadbent, G.C., 2007. Prolonged history of episodic fluid flow in giant hematite ore bodies: evidence from in situ U–Pb geochronology of hydrothermal xenotime. Earth Planet. Sci. Lett. 258, 249–259.

Rasmussen, B., Muhling, J., Krapež, B., 2021. Greenalite and its role in the genesis of early Precambrian iron formations–A review. Earth-Sci. Rev. 217, 103613.

Rasmussen, B., Zi, J.W., Sheppard, S., Krapež, B., Muhling, J.R., 2016. Multiple episodes of hematite mineralization indicated by U-Pb dating of iron-ore deposits, Marquette Range, Michigan, USA. Geology 44, 547–550. https://doi.org/10.1130/G37783.1.

Robbins, L.J., Funk, S.P., Flynn, S.L., Warchola, T.J., Li, Z., Lalonde, S.V., Rostron, B.J., Smith, A.J., Beukes, N.J., de Kock, M.O., et al., 2019. Hydrogeological constraints on the formation of Palaeoproterozoic banded iron formations. Nat. Geosci. 12, 558–563.

Runkel, A.C., McKay, R.M., Cowan, C.A., Miller, J.F., Taylor, J.F., 2012. The Sauk megasequence in the cratonic interior of North America: interplay between a fully developed inner detrital belt and the central great American carbonate bank. In: Great American Carbonate Bank: The Geology and Economic Resources of the Cambrian—Ordovician Sauk Megasequence of Laurentia. American Association of Petroleum Geologists.

Santos, J., Lobato, L., Figueiredo e Silva, R., Zuchetti, M., Fletcher, I., McNaughton, N., Hagemann, S., 2010. Two Statherian hydrothermal events in the Carajás Province: evidence from Pb–Pb SHRIMP and Pb–Th SHRIMP dating of hydrothermal anatase and monazite. In: VII SSAGI South American Symposium on Isotope Geology. Anais, CD-ROM, Brasília.

Schneider, D., Bickford, M., Cannon, W., Schulz, K., Hamilton, M., 2002. Age of volcanic rocks and syndepositional iron formations, Marquette range supergroup: implications for the tectonic setting of paleoproterozoic iron formations of the Lake Superior region. Can. J. Earth Sci. 39, 999–1012.

Schulz, K.J., Cannon, W.F., 2007. The Penokean orogeny in the Lake Superior region. Precambrian Res. 157, 4–25.

Figueiredo e Silva, R.C., Hagemann, S., Lobato, L.M., Rosière, C.A., Banks, D.A., Davidson, G.J., Vennemann, T., Hergt, J., 2013. Hydrothermal fluid processes and evolution of the giant Serra Norte jaspilite-hosted iron ore deposits, Carajás Mineral Province, Brazil. Econ. Geol. 108, 739–779.

Simmons, G.C., 1974. Bedrock geologic map of the Ishpeming quadrangle, Marquette County, Michigan. Technical Report. US Geological Survey.

Smith, G.L., Byers, C.W., Dott, R.H., Witzke, B., Ludvigson, G., Day, J., 1996. Sequence stratigraphy of the Prairie du Chien Group, lower Ordovician, Midcontinent, USA. Special Papers-Geological Society of America, 23–34.

Spier, C.A., Vasconcelos, P.M., Oliviera, S.M., 2006. $^{40}Ar/^{39}Ar$ geochronological constraints on the evolution of lateritic iron deposits in the Quadrilátero Ferrífero, Minas Gerais, Brazil. Chem. Geol. 234, 79–104.

Sturrock, C.P., Flowers, R.M., Kohn, B.P., Metcalf, J.R., 2024. Phanerozoic burial and erosion history of the southern Canadian shield from apatite (U-Th)/He thermochronology. Minerals 14, 57.

Swanson-Hysell, N.L., 2021. The Precambrian paleogeography of Laurentia. In: Ancient Supercontinents and the Paleogeography of Earth. Elsevier, pp. 109–153.

Swanson-Hysell, N.L., Feinberg, J.M., Berquó, T.S., Maloof, A.C., 2011. Self-reversed magnetization held by martite in basalt flows from the 1.1-billion-year-old Keweenawan rift, Canada. Earth Planet. Sci. Lett. 305, 171–184. https://doi.org/10.1016/j.epsl.2011.02.053.

Swanson-Hysell, N.L., Ramezani, J., Fairchild, L.M., Rose, I.R., 2019a. Failed rifting and fast drifting: Midcontinent Rift development, Laurentia's rapid motion and the driver of Grenvillian orogenesis. GSA Bull. 131, 913–940.

Swanson-Hysell, N.L., Fairchild, L.M., Slotznick, S.P., 2019b. Primary and secondary red bed magnetization constrained by fluvial intraclasts. J. Geophys. Res., Solid Earth 124, 4276–4289. https://doi.org/10.1029/2018jb017067.

Swanson-Hysell, N.L., Rivers, T., van der Lee, S., 2023. The late mesoproterozoic to early neoproterozoic Grenvillian orogeny and the assembly of Rodinia: turning point in the tectonic evolution of Laurentia. In: Laurentia: Turning Points in the Evolution of a Continent. Geological Society of America.

Symons, D., 1967a. A paleomagnetic study of concentrating iron ores from northern Michigan. Econ. Geol. 62, 118–137.

Symons, D., 1967b. Paleomagnetic evidence on the origin of the Marquette and Steep Rock hard hematite and goethite deposits. Can. J. Earth Sci. 4, 1–20.

Tasistro-Hart, A.R., Macdonald, F.A., 2023. Phanerozoic flooding of North America and the great unconformity. Proc. Natl. Acad. Sci. USA 120, e2309084120.

Tauxe, L., Shaar, R., Jonestrask, L., Swanson-Hysell, N., Minnett, R., Koppers, A., Constable, C., Jarboe, N., Gaastra, K., Fairchild, L., 2016. PmagPy: software package for paleomagnetic data analysis and a bridge to the magnetics information consortium (MagIC) database. Geochem. Geophys. Geosyst. 17, 2450–2463.

Tauxe, L., Watson, G., 1994. The fold test: an eigen analysis approach. Earth Planet. Sci. Lett. 122, 331–341. https://doi.org/10.1016/0012-821x(94)90006-x.

Thorne, W.S., Hagemann, S.G., Sepe, D., Dalstra, H.J., Banks, D.A., 2014. Structural control, hydrothermal alteration zonation, and fluid chemistry of the concealed, high-grade 4EE iron orebody at the Paraburdoo 4E deposit, Hamersley province. Econ. Geol. 109, 1529–1562.

Tohver, E., Holm, D., van Der Pluijm, B., Essene, E., Cambray, F., 2007. Late paleoproterozoic (geon 18 and 17) reactivation of the neoarchean Great Lakes tectonic zone, northern Michigan, USA: evidence from kinematic analysis, thermobarometry and 40Ar/39Ar geochronology. Precambrian Res. 157, 144–168.

Torsvik, T.H., Van der Voo, R., Preeden, U., Mac Niocaill, C., Steinberger, B., Doubrovine, P.V., van Hinsbergen, D.J.J., Domeier, M., Gaina, C., Tohver, E., Meert, J.G., McCausland, P.J.A., Cocks, L.R.M., 2012. Phanerozoic polar wander, palaeogeography and dynamics. Earth-Sci. Rev. 114, 325–368. https://doi.org/10.1016/j.earscirev.2012.06.007.

Vermeesch, P., 2018. IsoplotR: a free and open toolbox for geochronology. Geosci. Front. 9, 1479–1493. https://doi.org/10.1016/j.gsf.2018.04.001.

Watson, E.B., Cherniak, D.J., Nichols, C.I., Weiss, B.P., 2023. Pb diffusion in magnetite: dating magnetite crystallization and the timing of remanent magnetization in banded iron formation. Chem. Geol. 640, 121748.

Webb, P., Wiedenbeck, M., Glodny, J., 2020. G-Chron 2019–Round 1: An International Proficiency Test for U-Pb Geochronology Laboratories; Report on the 2019 Round of G-Chron based on Palaeozoic Zircon Rak-17 (Distribution: September 2019).

Wiedenbeck, M., Alle, P., Corfu, F., Griffin, W.L., Meier, M., Oberli, F.v., Quadt, A.v., Roddick, J., Spiegel, W., 1995. Three natural zircon standards for U-Th-Pb, Lu-Hf, trace element and REE analyses. Geostand. Newsl. 19, 1–23.

Wotte, T., Skovsted, C.B., Whitehouse, M.J., Kouchinsky, A., 2019. Isotopic evidence for temperate oceans during the Cambrian explosion. Sci. Rep. 9, 6330.

Zhang, Y., Hodgin, E.B., Alemu, T., Pierce, J., Fuentes, A., Swanson-Hysell, N.L., 2024. Tracking Rodinia into the neoproterozoic: new paleomagnetic constraints from the Jacobsville formation. Tectonics 43, e2023TC007866.

Zhao, J., Brugger, J., Pring, A., 2019. Mechanism and kinetics of hydrothermal replacement of magnetite by hematite. Geosci. Front. 10, 29–41.

Zi, J.W., Sheppard, S., Muhling, J.R., Rasmussen, B., 2022. Refining the paleoproterozoic tectonothermal history of the Penokean orogen: new U-Pb age constraints from the Pembine-Wausau terrane, Wisconsin, USA. GSA Bull. 134, 776–790.

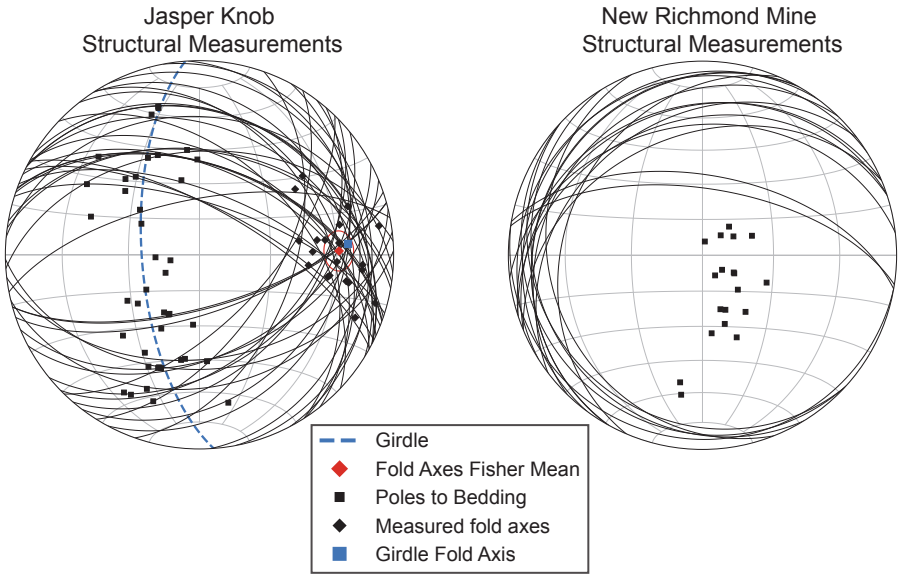

Figure S1: Structural measurements plotted on equal area stereonets spanning the jaspilite facies exposed at Jasper Knob and the New Richmond mine. The bedding plane measurements correspond to the strike and dip of the vibrant jasper and specularite laminations that define the folds. The trend and plunge of individual fold axes were taken where the fold axes of the tight, meter-scale folds were well-exposed at the summit of Jasper Knob. A Fisher mean of these fold axes defining an eastward plunging orientation is plotted with its 95% confidence ellipse. A best fit girdle to the poles of these bedding measurements was used to determine the fold limb-defined main fold axis which lies within the 95% confidence interval of the Fisher mean of the measured fold axes and is therefore indistinguishable. The New Richmond mine jaspilite was less tightly folded than the same facies exposed at Jasper Knob. Exposed bedding planes at the New Richmond mine have a shallower westerly dipping orientation in contrast to those at Jasper Knob. All structural measurements were taken using the FieldMove Clino application.

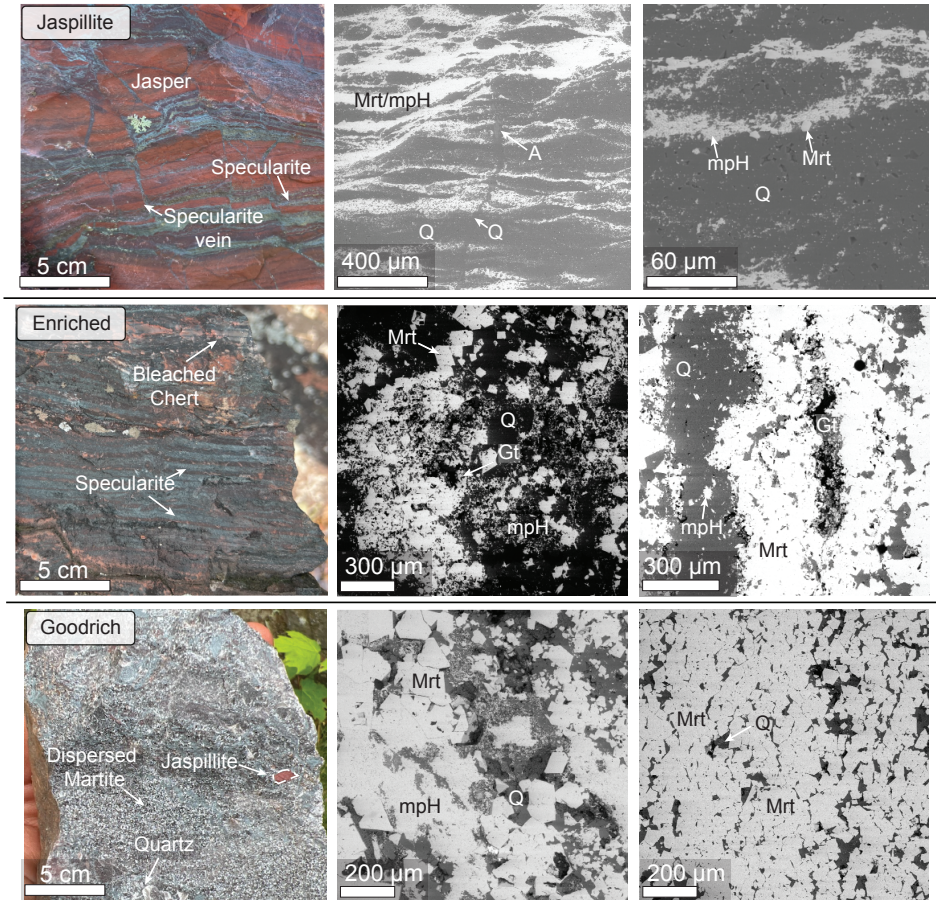

Figure S2: Field photographs and backscatter electron (BSE) images of the three iron oxide facies that were sampled. Representative field images for the jaspilite-facies, enriched-facies, and basal Goodrich conglomerate at Jasper Knob are shown in the first column at the start of each row. BSE images from specimens corresponding to each facies are on the same row as their respective field image. *(Upper Row)* Field photo of *in-situ* jaspilite at the summit of Jasper Knob illustrating textural complexity of this facies in the form of numerous cross-cutting specularite veins and brecciation. Bands of specularite in BSE images are composed of fine, bladed to microplaty hematite (mpH) with disseminated coarser grained martite (Mrt). Quartz (Q) in the jasper bands forms larger and more coherent bands in the jaspilite than in the enriched or conglomerate facies. A grain of apatite (A) in a cross-cutting quartz vein is a minor accessory phase. *(Middle Panel)* The enriched facies is noticeably more muted and specularite dominated in the field image, with the bright jasper bleached to pale white. The BSE images from samples JK23 show increased porosity that is infilled with botryoidal ferric oxides (likely goethite; Gt) and the martite grain boundaries are less apparent than in the jaspilite samples. *(Lower Panel)* The Goodrich Conglomerate as exposed near the contact with the Negaunee IF at Jasper Knob adjacent to a mine pit. The black, fine sand-sized flecks on the specimen in the field photo are disseminated grains of martite visible in the accompanying BSE images of dated specimen GQ6-2 that occur within a microcrystalline matrix of quartz. A red jasper clast is outlined by the dashed polygon. Fibrous microplaty hematite forms large masses that surround martite grains. The microplaty hematite has sharp contacts with intact martite grains in the middle BSE image while in other places appears to have dissolved adjacent martite. The BSE image in the lower right shows the disseminated martite that forms the main oxide texture. These martite grains were too uranium-poor with too limited of a compositional spread to be dated.

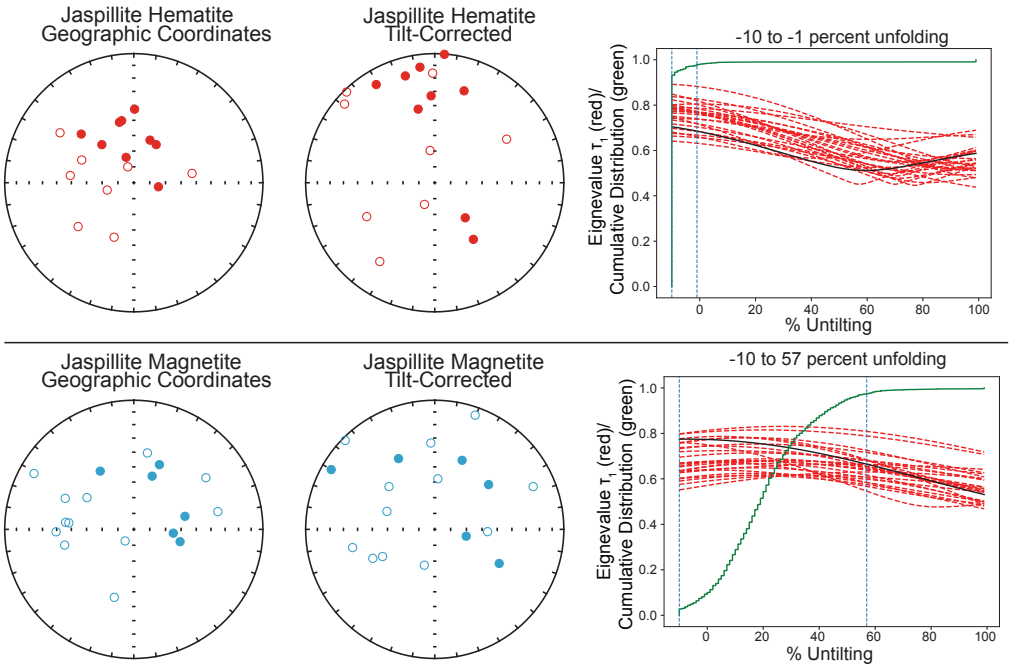

Figure S3: Jaspilite facies fold test results for both the hematite *upper panel* and magnetite *lower panel* components isolated from specimens collected at the summit of Jasper Knob. Geographic and tilt corrected directions are plotted for each component. The hematite and magnetite fit directions become more dispersed visually after correcting for the dip of the laminations. To the right of the equal area plots are the results of bootstrap fold test of ref.Tauxe and Watson (1994) for each set of directional data. The tightest cluster of directions (peak of black curve and of red dashed bootstrap resamples summarized by the green CDF curve) is achieved prior to application of a structural correction in the case of the hematite component. The magnetite directions likewise fail the fold test.

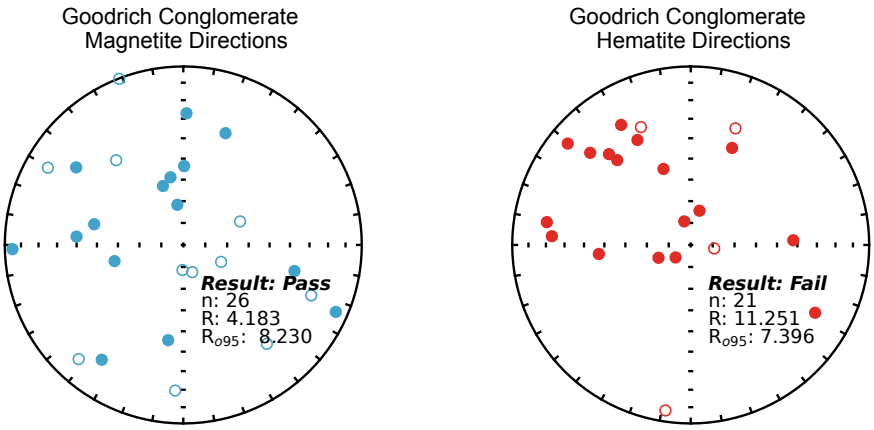

Figure S4: Results for the conglomerate tests conducted on the magnetite(*left*) and hematite (*right*) components isolated from specimens of iron formation clasts incorporated within the basal Goodrich conglomerate. The equal area plots show both components, in geographic coordinates, from specimens with interpretable demagnetization behavior. The data shown in the hematite equal area are identical to Fig. 2B in the main text. In contrast to the results of the conglomerate test on the hematite component, the *magnetite* component exhibits an $R < R_o$ at the 95% confidence level indicating that the data are not distinguishable from random directions and therefore pass a conglomerate test. The magnetite directions are much more highly dispersed than the hematite directions but this may be a product of the polyphase development of magnetite that has been acknowledged in other ore deposits Angerer et al. (2021). The results of the field tests cannot inform the original oxide mineralogy of the protolith clasts aside from hosting iron rich phases, as the petrographical observations show that these units are profoundly recrystallized.

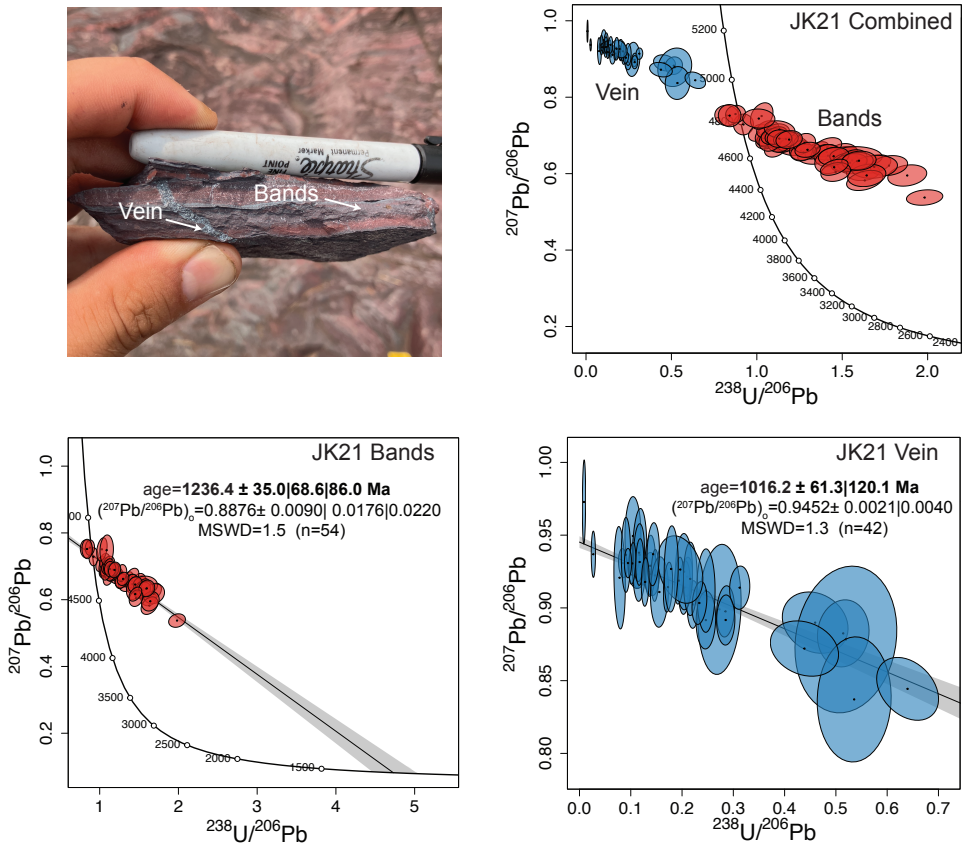

Figure S5: Jaspilite facies specimen JK21 collected for paired paleomagnetic and U/Pb analyses. Upper right panel is a field image of JK21 with jaspilite texture cross cut by a coarse specularite vein composed of fine-sand sized specularite crystals. The upper left is a Tera-Wasserburg plot showing spots collected on cross-cutting vein hematite grains (blue) and from martite grains forming the specularite bands within the jaspilite texture. It is evident that the vein data is following a different linear array that has a shallower slope than the jaspilite martite data which has a steeper slope consistent with the difference in texture between the two textures and cross cutting relationship. The lower left panel shows only the U/Pb data from the jaspilite band hematite that yield an older age than the cross-cutting vein which is expected given the vein cuts the jaspilite and is far coarser. The vein data is plotted in the lower right and has low $^{238}U/^{206}Pb$ values that plot to the left of concordia but has enough spread to elucidate a younger trajectory than the jaspilite martite.

References

Angerer, T., Hagemann, S.G., Walde, D.H., 2021. Diagenetic and supergene ore forming processes in the iron formation of the Neoproterozoic Jacadigo Group, Corumbá, Brazil. Journal of South American Earth Sciences 105, 102902.

Tauxe, L., Watson, G., 1994. The fold test: an eigen analysis approach. Earth and Planetary Science Letters 122, 331–341. URL: http://dx.doi.org/10.1016/0012-821x(94)90006-x, doi:10.1016/0012-821x(94)90006-x.

Supplementary Table S1. LA-ICP-MS U-Pb geochronologic analyses for all samples and RMs. All standard errors reported at 2σ. Zircon RMs and unknowns normalized to HFO hematite RM.

	Spot Size (µm)	$^{238}U/^{206}Pb$	$^{238}U/^{206}Pb$ 2SE(int)	$^{238}U/^{206}Pb$ 2SE(prop)	$^{206}Pb/^{238}U$	$^{206}Pb/^{238}U$ 2SE(int)	$^{206}Pb/^{238}U$ 2SE(prop)	$^{207}Pb/^{235}U$	$^{207}Pb/^{235}U$ 2SE(int)	$^{207}Pb/^{235}U$ 2SE(prop)	$^{207}Pb/^{206}Pb$	$^{207}Pb/^{206}Pb$ 2SE(int)	$^{207}Pb/^{206}Pb$ 2SE(prop)	Err Corr 7/6 v 8/6	Err Corr 6/8 v 7/5
HFO- Hematite(Day 1)															
HFO-1	60	8.196	0.047	0.240	0.122	0.001	0.004	15.406	0.083	0.442	0.917	0.004	0.004	0.446	0.729
HFO-10	60	8.172	0.043	0.234	0.122	0.001	0.004	15.447	0.081	0.439	0.917	0.004	0.005	0.439	0.610
HFO-11	60	8.179	0.041	0.238	0.122	0.001	0.004	15.438	0.074	0.441	0.917	0.004	0.004	0.486	0.640
HFO-12	60	8.194	0.040	0.240	0.122	0.001	0.004	15.408	0.072	0.437	0.917	0.004	0.005	0.548	0.437
HFO-13	60	8.195	0.062	0.250	0.122	0.001	0.004	15.405	0.102	0.444	0.917	0.006	0.006	0.474	0.656
HFO-14	60	8.154	0.040	0.234	0.123	0.001	0.004	15.485	0.081	0.440	0.917	0.005	0.005	0.507	0.509
HFO-15	60	8.210	0.039	0.230	0.122	0.001	0.004	15.377	0.072	0.444	0.917	0.004	0.005	0.603	0.599
HFO-16	60	8.192	0.042	0.237	0.122	0.001	0.004	15.407	0.082	0.440	0.916	0.003	0.004	0.339	0.785
HFO-17	60	8.195	0.041	0.246	0.122	0.001	0.004	15.427	0.082	0.448	0.917	0.004	0.004	0.312	0.678
HFO-18	60	8.175	0.043	0.235	0.122	0.001	0.004	15.437	0.081	0.442	0.916	0.004	0.005	0.432	0.611
HFO-19	60	8.184	0.054	0.240	0.122	0.001	0.004	15.427	0.109	0.451	0.917	0.005	0.005	0.400	0.709
HFO-2	60	8.158	0.033	0.228	0.123	0.001	0.003	15.474	0.067	0.432	0.917	0.003	0.004	0.382	0.640
HFO-20	60	8.184	0.048	0.243	0.122	0.001	0.004	15.426	0.092	0.448	0.917	0.004	0.005	0.435	0.661
HFO-21	60	8.190	0.048	0.244	0.122	0.001	0.004	15.418	0.093	0.448	0.917	0.005	0.005	0.478	0.618
HFO-22	60	8.184	0.068	0.248	0.122	0.001	0.004	15.431	0.128	0.456	0.917	0.006	0.006	0.360	0.707
HFO-23	60	8.188	0.056	0.254	0.122	0.001	0.004	15.420	0.109	0.453	0.917	0.005	0.006	0.457	0.612
HFO-24	60	8.186	0.046	0.240	0.122	0.001	0.004	15.422	0.087	0.445	0.917	0.005	0.006	0.555	0.512
HFO-25	60	8.189	0.046	0.241	0.122	0.001	0.004	15.419	0.086	0.445	0.917	0.005	0.005	0.482	0.581
HFO-26	60	8.180	0.047	0.242	0.122	0.001	0.004	15.437	0.084	0.444	0.917	0.004	0.005	0.491	0.647
HFO-27	60	8.190	0.048	0.242	0.122	0.001	0.004	15.415	0.090	0.446	0.917	0.004	0.005	0.410	0.715
HFO-28	60	8.189	0.056	0.240	0.122	0.001	0.004	15.423	0.106	0.449	0.917	0.005	0.005	0.384	0.716
HFO-29	60	8.179	0.047	0.232	0.122	0.001	0.004	15.429	0.090	0.445	0.916	0.004	0.005	0.464	0.593
HFO-3	60	8.203	0.037	0.239	0.122	0.001	0.004	15.389	0.067	0.434	0.917	0.004	0.005	0.538	0.473
HFO-30	60	8.190	0.040	0.242	0.122	0.001	0.004	15.418	0.072	0.443	0.917	0.004	0.004	0.496	0.678
HFO-31	60	8.189	0.050	0.235	0.122	0.001	0.004	15.424	0.101	0.447	0.917	0.005	0.006	0.449	0.594
HFO-32	60	8.188	0.059	0.240	0.122	0.001	0.004	15.409	0.103	0.444	0.916	0.006	0.006	0.458	0.536
HFO-33	60	8.181	0.053	0.239	0.122	0.001	0.004	15.440	0.100	0.448	0.917	0.006	0.006	0.535	0.496
HFO-34	60	8.199	0.049	0.243	0.122	0.001	0.004	15.397	0.080	0.444	0.917	0.004	0.005	0.600	0.701
HFO-35	60	8.170	0.046	0.248	0.122	0.001	0.004	15.436	0.078	0.430	0.917	0.005	0.005	0.556	0.554
HFO-36	60	8.190	0.039	0.238	0.122	0.001	0.004	15.418	0.079	0.444	0.917	0.005	0.005	0.483	0.505
HFO-37	60	8.200	0.050	0.243	0.122	0.001	0.004	15.400	0.089	0.449	0.917	0.004	0.005	0.445	0.705
HFO-38	60	8.179	0.044	0.245	0.122	0.001	0.004	15.428	0.083	0.444	0.917	0.005	0.005	0.518	0.540
HFO-39	60	8.174	0.044	0.236	0.122	0.001	0.004	15.441	0.085	0.441	0.916	0.005	0.005	0.410	0.584
HFO-4	60	8.186	0.038	0.235	0.122	0.001	0.004	15.425	0.070	0.442	0.917	0.004	0.004	0.550	0.555
HFO-40	60	8.172	0.050	0.236	0.122	0.001	0.004	15.449	0.083	0.437	0.917	0.004	0.005	0.533	0.650
HFO-41	60	8.186	0.045	0.227	0.122	0.001	0.003	15.424	0.084	0.421	0.917	0.004	0.004	0.405	0.754
HFO-42	60	8.198	0.044	0.238	0.122	0.001	0.003	15.397	0.085	0.437	0.916	0.004	0.005	0.400	0.636
HFO-43	60	8.183	0.039	0.240	0.122	0.001	0.004	15.426	0.083	0.444	0.917	0.004	0.005	0.332	0.597
HFO-44	60	8.192	0.036	0.231	0.122	0.001	0.004	15.415	0.068	0.443	0.917	0.004	0.004	0.523	0.638
HFO-45	60	8.182	0.051	0.235	0.122	0.001	0.004	15.432	0.091	0.450	0.917	0.004	0.005	0.415	0.724
HFO-46	60	8.183	0.052	0.238	0.122	0.001	0.004	15.426	0.094	0.445	0.916	0.004	0.005	0.406	0.744
HFO-47	60	8.182	0.045	0.234	0.122	0.001	0.004	15.434	0.084	0.436	0.917	0.004	0.005	0.400	0.678
HFO-48	60	8.198	0.041	0.236	0.122	0.001	0.003	15.410	0.079	0.439	0.917	0.004	0.005	0.451	0.681
HFO-5	60	8.180	0.034	0.226	0.122	0.001	0.004	15.429	0.068	0.440	0.916	0.004	0.005	0.536	0.385
HFO-52	60	8.189	0.043	0.244	0.122	0.001	0.004	15.419	0.075	0.440	0.917	0.004	0.005	0.490	0.689
HFO-53	60	8.176	0.039	0.238	0.122	0.001	0.004	15.442	0.076	0.448	0.917	0.004	0.004	0.476	0.707
HFO-54	60	8.190	0.039	0.235	0.122	0.001	0.004	15.415	0.068	0.437	0.917	0.003	0.004	0.510	0.751
HFO-6	60	8.191	0.035	0.238	0.122	0.001	0.004	15.418	0.065	0.440	0.917	0.003	0.004	0.479	0.703
HFO-7	60	8.198	0.038	0.242	0.122	0.001	0.004	15.402	0.070	0.435	0.917	0.004	0.005	0.560	0.532
HFO-78	60	8.197	0.047	0.236	0.122	0.001	0.004	15.403	0.091	0.437	0.917	0.004	0.005	0.442	0.628
HFO-8	60	8.167	0.034	0.233	0.122	0.001	0.004	15.456	0.069	0.443	0.917	0.004	0.004	0.433	0.565
HFO-9	60	8.191	0.037	0.239	0.122	0.001	0.004	15.414	0.067	0.442	0.917	0.004	0.004	0.496	0.575
HFO- Hematite (Day 2)															
HFO - 1	60	8.192	0.079	0.212	0.122	0.001	0.003	2840.665	8.868	23.758	0.917	0.010	0.011	0.590	0.378
HFO - 10	60	8.183	0.075	0.207	0.122	0.001	0.003	2842.214	8.567	23.655	0.917	0.007	0.009	0.506	0.679
HFO - 11	60	8.188	0.062	0.205	0.122	0.001	0.003	2840.716	6.193	22.428	0.917	0.007	0.009	0.619	0.454
HFO - 12	60	8.190	0.064	0.205	0.122	0.001	0.003	2841.344	7.515	23.421	0.917	0.006	0.009	0.430	0.616
HFO - 13	60	8.186	0.059	0.205	0.122	0.001	0.003	2840.992	6.834	22.522	0.917	0.005	0.008	0.382	0.667
HFO - 14	60	8.192	0.056	0.202	0.122	0.001	0.003	2840.414	6.287	22.243	0.917	0.005	0.008	0.415	0.703
HFO - 15	60	8.178	0.055	0.204	0.122	0.001	0.003	2842.001	6.168	22.237	0.917	0.005	0.008	0.371	0.678
HFO - 16	60	8.184	0.081	0.212	0.122	0.001	0.003	2840.074	10.095	23.663	0.917	0.010	0.012	0.571	0.367
HFO - 17	60	8.196	0.072	0.205	0.122	0.001	0.003	2838.781	9.584	23.400	0.917	0.009	0.011	0.504	0.446
HFO - 18	60	8.173	0.077	0.208	0.122	0.001	0.003	2841.668	10.682	23.927	0.917	0.010	0.012	0.418	0.418
HFO - 19	60	8.186	0.076	0.206	0.122	0.001	0.003	2840.125	10.486	23.880	0.917	0.011	0.012	0.479	0.463
HFO - 2	60	8.176	0.087	0.209	0.122	0.001	0.003	2841.581	10.062	23.536	0.917	0.010	0.012	0.535	0.420
HFO - 20	60	8.191	0.083	0.209	0.122	0.001	0.003	2839.403	9.599	23.570	0.917	0.009	0.011	0.458	0.574
HFO - 21	60	8.178	0.083	0.208	0.122	0.001	0.003	2840.768	9.875	23.664	0.917	0.008	0.010	0.372	0.590
HFO - 22	60	8.186	0.089	0.218	0.122	0.001	0.003	2839.548	10.597	23.981	0.916	0.009	0.011	0.410	0.568
HFO - 23	60	8.190	0.089	0.219	0.122	0.001	0.003	2839.787	9.876	23.579	0.917	0.010	0.012	0.512	0.443
HFO - 24	60	8.179	0.074	0.211	0.122	0.001	0.003	2842.087	10.983	24.436	0.917	0.010	0.011	0.342	0.558
HFO - 25	60	8.171	0.086	0.199	0.123	0.001	0.003	2843.800	10.899	23.453	0.917	0.009	0.011	0.486	0.610

HFO - 26	60	8.182	0.101	0.219	0.122	0.001	0.003	2840.334	11.662	24.331	0.917	0.010	0.012	0.493	0.634
HFO - 27	60	8.183	0.092	0.217	0.122	0.001	0.003	2840.979	10.130	23.859	0.917	0.009	0.011	0.490	0.591
HFO - 28	60	8.192	0.089	0.216	0.122	0.001	0.003	2838.123	11.621	24.623	0.916	0.010	0.012	0.435	0.528
HFO - 29	60	8.185	0.083	0.217	0.122	0.001	0.003	2839.978	10.071	23.792	0.917	0.009	0.011	0.435	0.516
HFO - 3	60	8.189	0.077	0.202	0.122	0.001	0.003	2839.588	9.430	23.353	0.917	0.010	0.012	0.571	0.393
HFO - 30	60	8.195	0.076	0.203	0.122	0.001	0.003	2840.542	9.572	23.799	0.917	0.009	0.011	0.523	0.500
HFO - 31	60	8.171	0.075	0.210	0.122	0.001	0.003	2842.209	8.968	22.493	0.916	0.009	0.011	0.502	0.510
HFO - 32	60	8.187	0.079	0.206	0.122	0.001	0.003	2840.186	11.317	24.239	0.917	0.009	0.011	0.266	0.584
HFO - 33	60	8.183	0.082	0.210	0.122	0.001	0.003	2840.115	10.154	23.719	0.917	0.009	0.011	0.413	0.492
HFO - 34	60	8.185	0.079	0.209	0.122	0.001	0.003	2841.099	9.011	23.166	0.917	0.009	0.011	0.539	0.448
HFO - 35	60	8.193	0.075	0.205	0.122	0.001	0.003	2838.803	10.113	23.768	0.917	0.009	0.011	0.425	0.468
HFO - 36	60	8.182	0.084	0.214	0.122	0.001	0.003	2840.224	10.642	23.892	0.917	0.009	0.011	0.360	0.536
HFO - 37	60	8.190	0.080	0.209	0.122	0.001	0.003	2839.620	9.951	23.442	0.917	0.008	0.010	0.284	0.625
HFO - 38	60	8.189	0.082	0.215	0.122	0.001	0.003	2840.031	9.587	23.443	0.917	0.009	0.011	0.418	0.559
HFO - 39	60	8.190	0.091	0.214	0.122	0.001	0.003	2839.617	10.995	24.183	0.917	0.009	0.011	0.431	0.599
HFO - 4	60	8.191	0.050	0.206	0.122	0.001	0.003	2840.767	5.450	22.103	0.917	0.005	0.008	0.439	0.596
HFO - 40	60	8.176	0.080	0.208	0.122	0.001	0.003	2840.738	9.854	23.597	0.916	0.008	0.010	0.459	0.603
HFO - 41	60	8.191	0.093	0.218	0.122	0.001	0.003	2838.504	12.032	24.516	0.917	0.009	0.011	0.328	0.638
HFO - 42	60	8.191	0.084	0.212	0.122	0.001	0.003	2839.927	10.588	23.870	0.918	0.009	0.011	0.376	0.590
HFO - 43	60	8.177	0.101	0.222	0.122	0.001	0.003	2838.814	11.716	24.596	0.915	0.010	0.011	0.397	0.614
HFO - 44	60	8.191	0.067	0.201	0.122	0.001	0.003	2840.392	8.454	23.251	0.917	0.009	0.011	0.485	0.396
HFO - 45	60	8.188	0.082	0.211	0.122	0.001	0.003	2841.638	10.965	23.659	0.918	0.010	0.012	0.341	0.481
HFO - 46	60	8.177	0.083	0.208	0.122	0.001	0.003	2841.723	10.604	24.520	0.916	0.009	0.011	0.331	0.573
HFO - 47	60	8.205	0.090	0.218	0.122	0.001	0.003	2838.729	10.012	23.723	0.918	0.009	0.011	0.390	0.598
HFO - 48	60	8.175	0.075	0.208	0.122	0.001	0.003	2841.053	9.453	23.391	0.916	0.009	0.011	0.423	0.448
HFO - 49	60	8.192	0.068	0.204	0.122	0.001	0.003	2840.282	8.716	23.046	0.917	0.009	0.011	0.354	0.444
HFO - 5	60	8.169	0.063	0.204	0.122	0.001	0.003	2842.358	6.574	22.354	0.916	0.004	0.008	0.346	0.780
HFO - 50	60	8.173	0.065	0.202	0.122	0.001	0.003	2841.237	8.454	23.068	0.916	0.008	0.010	0.330	0.499
HFO - 51	60	8.193	0.064	0.210	0.122	0.001	0.003	2840.131	7.949	22.858	0.917	0.007	0.009	0.452	0.483
HFO - 52	60	8.190	0.067	0.202	0.122	0.001	0.003	2839.859	9.571	23.521	0.917	0.008	0.010	0.385	0.505
HFO - 53	60	8.177	0.074	0.203	0.122	0.001	0.003	2840.701	10.407	23.860	0.917	0.009	0.011	0.351	0.545
HFO - 54	60	8.190	0.073	0.207	0.122	0.001	0.003	2840.872	9.962	24.059	0.917	0.008	0.010	0.405	0.591
HFO - 55	60	8.191	0.112	0.223	0.122	0.002	0.003	2838.416	13.542	25.567	0.917	0.010	0.012	0.315	0.671
HFO - 56	60	8.177	0.097	0.226	0.122	0.001	0.003	2839.831	11.869	24.506	0.916	0.010	0.011	0.302	0.615
HFO - 57	60	8.190	0.100	0.219	0.122	0.001	0.003	2839.196	11.220	24.313	0.917	0.009	0.011	0.446	0.608
HFO - 58	60	8.176	0.102	0.216	0.122	0.002	0.003	2840.433	11.822	24.285	0.917	0.010	0.012	0.404	0.581
HFO - 59	60	8.215	0.089	0.211	0.122	0.001	0.003	2837.817	11.784	25.119	0.917	0.009	0.011	0.338	0.640
HFO - 6	60	8.199	0.052	0.204	0.122	0.001	0.003	2840.577	5.271	22.254	0.917	0.005	0.008	0.578	0.476
HFO - 60	60	8.163	0.090	0.212	0.123	0.001	0.003	2842.453	9.732	23.657	0.916	0.010	0.012	0.487	0.463
HFO - 61	60	8.180	0.082	0.203	0.122	0.001	0.003	2839.564	10.609	24.086	0.916	0.009	0.011	0.310	0.550
HFO - 62	60	8.186	0.077	0.209	0.122	0.001	0.003	2840.552	10.257	23.669	0.917	0.008	0.010	0.228	0.594
HFO - 63	60	8.172	0.087	0.207	0.122	0.001	0.003	2839.376	11.142	24.092	0.916	0.010	0.012	0.427	0.540
HFO - 64	60	8.191	0.083	0.215	0.122	0.001	0.003	2842.149	9.967	24.417	0.918	0.010	0.012	0.518	0.437
HFO - 65	60	8.182	0.073	0.200	0.122	0.001	0.003	2840.695	10.508	24.381	0.916	0.009	0.011	0.402	0.521
HFO - 66	60	8.177	0.083	0.212	0.122	0.001	0.003	2840.220	11.360	24.419	0.916	0.010	0.011	0.363	0.582
HFO - 67	60	8.198	0.103	0.222	0.122	0.001	0.003	2837.485	13.416	25.264	0.917	0.010	0.012	0.301	0.634
HFO - 68	60	8.188	0.087	0.208	0.122	0.001	0.003	2839.899	11.046	24.278	0.917	0.010	0.012	0.427	0.495
HFO - 69	60	8.189	0.107	0.222	0.122	0.002	0.003	2841.875	11.416	23.719	0.917	0.010	0.012	0.457	0.594
HFO - 7	60	8.187	0.059	0.207	0.122	0.001	0.003	2840.736	6.243	22.325	0.917	0.005	0.008	0.394	0.555
HFO - 70	60	8.205	0.112	0.224	0.122	0.002	0.003	2836.492	12.658	24.870	0.916	0.009	0.011	0.386	0.715
HFO - 71	60	8.181	0.083	0.207	0.122	0.001	0.003	2840.717	11.215	24.332	0.917	0.009	0.011	0.338	0.575
HFO - 72	60	8.184	0.073	0.208	0.122	0.001	0.003	2841.240	8.077	22.911	0.917	0.005	0.008	0.291	0.777
HFO - 73	60	8.187	0.053	0.201	0.122	0.001	0.003	2841.548	5.744	21.350	0.917	0.004	0.007	0.310	0.696
HFO - 74	60	8.194	0.060	0.204	0.122	0.001	0.003	2839.645	5.739	22.523	0.916	0.004	0.007	0.343	0.712
HFO - 75	60	8.172	0.055	0.197	0.122	0.001	0.003	2842.331	6.252	22.527	0.917	0.004	0.007	0.238	0.705
HFO - 76	60	8.213	0.102	0.227	0.122	0.001	0.003	2837.829	12.287	25.236	0.917	0.010	0.012	0.479	0.708
HFO - 77	60	8.195	0.095	0.217	0.122	0.001	0.003	2838.810	10.434	23.488	0.917	0.009	0.011	0.487	0.598
HFO - 78	60	8.170	0.067	0.206	0.122	0.001	0.003	2841.696	9.975	23.720	0.917	0.010	0.011	0.397	0.387
HFO - 79	60	8.191	0.100	0.220	0.122	0.001	0.003	2837.972	12.358	24.721	0.916	0.011	0.012	0.372	0.540
HFO - 8	60	8.189	0.062	0.204	0.122	0.001	0.003	2841.549	6.165	22.401	0.917	0.005	0.008	0.441	0.677
HFO - 9	60	8.179	0.060	0.199	0.122	0.001	0.003	2842.020	6.020	21.746	0.916	0.005	0.008	0.483	0.634
Z_91500- Zircon (Day 1)															
91500-1	30	6.408	0.042	0.182	0.156	0.001	0.005	1.600	0.031	0.055	0.075	0.001	0.002	0.257	0.071
91500-10	30	6.390	0.064	0.197	0.157	0.002	0.005	1.607	0.036	0.058	0.074	0.002	0.002	0.179	0.273
91500-11	30	6.750	0.057	0.195	0.148	0.001	0.004	1.503	0.032	0.053	0.073	0.001	0.001	0.072	0.348
91500-12	30	6.696	0.066	0.211	0.150	0.001	0.005	1.522	0.034	0.055	0.074	0.002	0.002	0.268	0.154
91500-14	30	6.631	0.071	0.200	0.151	0.002	0.005	1.579	0.035	0.056	0.076	0.001	0.002	0.097	0.425
91500-15	30	6.667	0.062	0.198	0.150	0.001	0.005	1.573	0.031	0.054	0.076	0.001	0.001	0.100	0.403
91500-16	30	6.688	0.060	0.200	0.150	0.001	0.005	1.526	0.028	0.052	0.074	0.001	0.001	0.214	0.258
91500-17	30	6.492	0.063	0.197	0.154	0.001	0.005	1.571	0.031	0.054	0.074	0.001	0.001	0.141	0.336
91500-19	30	6.601	0.063	0.198	0.152	0.001	0.005	1.559	0.034	0.056	0.075	0.002	0.002	0.284	0.132
91500-2	30	6.624	0.060	0.202	0.151	0.001	0.005	1.551	0.029	0.052	0.074	0.001	0.001	0.259	0.223
91500-20	30	6.662	0.068	0.205	0.151	0.002	0.005	1.535	0.035	0.056	0.074	0.002	0.002	0.152	0.291
91500-21	30	6.746	0.063	0.206	0.149	0.001	0.004	1.547	0.032	0.054	0.076	0.002	0.002	0.219	0.231
91500-22	30	6.798	0.061	0.204	0.147	0.001	0.004	1.515	0.034	0.055	0.075	0.002	0.002	0.224	0.186
91500-24	30	6.473	0.069	0.196	0.155	0.002	0.005	1.596	0.033	0.056	0.075	0.001	0.001	0.079	0.464
91500-25	30	6.752	0.067	0.210	0.149	0.001	0.005	1.503	0.031	0.053	0.074	0.002	0.002	0.154	0.290
91500-26	30	6.718	0.064	0.201	0.149	0.001	0.005	1.530	0.029	0.052	0.074	0.001	0.001	0.154	0.365
91500-27	30	6.660	0.056	0.200	0.150	0.001	0.004	1.541	0.029	0.052	0.074	0.001	0.001	0.105	0.328

91500-29	30	6.759	0.068	0.210	0.148	0.001	0.005	1.531	0.036	0.056	0.075	0.002	0.002	0.205	0.208
91500-3	30	6.684	0.061	0.203	0.150	0.001	0.005	1.536	0.031	0.053	0.075	0.002	0.002	0.289	0.172
91500-30	30	6.710	0.064	0.204	0.149	0.001	0.005	1.546	0.037	0.057	0.075	0.002	0.002	0.222	0.204
91500-31	30	6.529	0.074	0.204	0.154	0.002	0.005	1.580	0.034	0.056	0.075	0.002	0.002	0.337	0.117
91500-32	30	6.590	0.069	0.200	0.152	0.002	0.005	1.584	0.036	0.058	0.076	0.002	0.002	0.119	0.290
91500-35	30	6.909	0.066	0.204	0.145	0.001	0.004	1.500	0.030	0.052	0.075	0.002	0.002	0.223	0.275
91500-36	30	6.768	0.064	0.207	0.148	0.001	0.004	1.550	0.030	0.053	0.076	0.001	0.001	0.156	0.334
91500-4	30	6.711	0.061	0.199	0.149	0.001	0.005	1.542	0.028	0.052	0.075	0.001	0.001	0.239	0.253
91500-5	30	6.733	0.057	0.202	0.149	0.001	0.004	1.529	0.028	0.051	0.075	0.001	0.001	0.113	0.362
91500-6	30	6.803	0.060	0.203	0.147	0.001	0.004	1.534	0.027	0.051	0.075	0.001	0.001	0.216	0.307
91500-7	30	6.768	0.050	0.204	0.148	0.001	0.004	1.497	0.026	0.050	0.073	0.001	0.001	0.230	0.202
91500-8	30	6.783	0.049	0.203	0.148	0.001	0.004	1.533	0.024	0.049	0.075	0.001	0.001	0.129	0.349
91500-9	30	6.453	0.064	0.197	0.156	0.002	0.005	1.581	0.036	0.057	0.074	0.002	0.002	0.271	0.154
Z_91500- Zircon (Day 2)															
91500-1	60	6.427	0.045	0.158	0.156	0.001	0.004	970.619	8.644	16.163	0.075	0.001	0.001	0.131	0.396
91500-10	60	6.588	0.076	0.172	0.152	0.002	0.004	960.633	10.666	17.560	0.075	0.001	0.001	0.209	0.519
91500-11	60	6.768	0.079	0.180	0.148	0.002	0.004	937.176	12.202	18.435	0.074	0.001	0.001	0.210	0.451
91500-12	60	6.765	0.091	0.184	0.148	0.002	0.004	936.880	11.910	18.215	0.075	0.001	0.001	0.316	0.419
91500-13	60	6.908	0.082	0.181	0.145	0.002	0.004	920.651	12.433	18.418	0.074	0.001	0.001	0.093	0.536
91500-14	60	6.955	0.084	0.184	0.144	0.002	0.004	920.555	13.164	19.029	0.075	0.001	0.001	0.105	0.478
91500-15	60	6.935	0.087	0.183	0.145	0.002	0.004	922.389	11.728	18.068	0.075	0.001	0.001	0.265	0.423
91500-16	60	6.845	0.087	0.181	0.146	0.002	0.004	932.453	12.862	18.846	0.075	0.001	0.002	0.268	0.405
91500-17	60	6.422	0.066	0.165	0.156	0.002	0.004	974.769	10.024	17.259	0.075	0.001	0.001	0.201	0.490
91500-18	60	6.597	0.084	0.177	0.152	0.002	0.004	957.541	12.511	18.774	0.075	0.001	0.001	0.157	0.516
91500-19	60	6.587	0.085	0.181	0.152	0.002	0.004	964.911	11.326	18.019	0.076	0.001	0.001	0.349	0.422
91500-2	60	6.434	0.072	0.169	0.156	0.002	0.004	973.406	10.905	17.805	0.075	0.001	0.001	0.092	0.562
91500-20	60	6.561	0.081	0.178	0.153	0.002	0.004	953.846	13.071	19.143	0.074	0.001	0.001	0.225	0.412
91500-21	60	6.570	0.084	0.178	0.153	0.002	0.004	953.521	11.441	18.066	0.074	0.001	0.001	0.161	0.555
91500-22	60	6.642	0.084	0.176	0.151	0.002	0.004	953.483	12.835	19.018	0.075	0.001	0.001	0.194	0.467
91500-23	60	6.699	0.086	0.179	0.150	0.002	0.004	953.838	12.384	18.642	0.076	0.001	0.001	0.223	0.473
91500-24	60	6.612	0.084	0.177	0.152	0.002	0.004	950.857	11.729	18.168	0.075	0.001	0.001	0.237	0.429
91500-25	60	6.642	0.075	0.175	0.151	0.002	0.004	954.376	12.678	18.525	0.075	0.001	0.001	0.211	0.385
91500-26	60	6.816	0.102	0.189	0.147	0.002	0.004	929.696	12.033	18.265	0.074	0.001	0.001	0.310	0.461
91500-27	60	6.843	0.101	0.189	0.147	0.002	0.004	940.087	12.716	18.707	0.076	0.001	0.001	0.270	0.481
91500-28	60	6.696	0.097	0.186	0.150	0.002	0.004	948.144	12.018	18.456	0.075	0.001	0.001	0.318	0.467
91500-29	60	6.663	0.088	0.182	0.151	0.002	0.004	941.191	11.758	17.780	0.074	0.001	0.001	0.222	0.469
91500-3	60	6.448	0.060	0.162	0.155	0.001	0.004	960.310	10.056	17.260	0.074	0.001	0.001	0.204	0.410
91500-30	60	6.816	0.073	0.175	0.147	0.002	0.004	935.070	13.158	19.038	0.075	0.001	0.002	0.171	0.366
91500-31	60	6.850	0.085	0.182	0.146	0.002	0.004	941.074	12.763	18.688	0.076	0.001	0.001	0.113	0.474
91500-32	60	6.842	0.081	0.180	0.147	0.002	0.004	939.921	12.059	18.348	0.076	0.001	0.002	0.220	0.389
91500-33	60	6.753	0.076	0.171	0.148	0.002	0.004	938.073	12.195	18.609	0.075	0.001	0.001	0.160	0.482
91500-34	60	6.882	0.081	0.178	0.146	0.002	0.004	933.103	12.942	18.874	0.075	0.001	0.001	0.159	0.417
91500-35	60	6.823	0.087	0.186	0.147	0.002	0.004	930.930	12.159	18.397	0.074	0.001	0.001	0.176	0.495
91500-36	60	6.790	0.078	0.177	0.147	0.002	0.004	929.531	12.064	18.239	0.074	0.001	0.001	0.256	0.354
91500-37	60	6.844	0.082	0.179	0.146	0.002	0.004	936.275	12.603	18.701	0.075	0.001	0.001	0.180	0.464
91500-38	60	6.825	0.079	0.179	0.147	0.002	0.004	930.171	12.013	18.298	0.075	0.001	0.002	0.290	0.336
91500-39	60	6.831	0.086	0.183	0.147	0.002	0.004	915.754	12.015	18.042	0.073	0.001	0.001	0.180	0.448
91500-4	60	6.513	0.061	0.164	0.154	0.001	0.004	969.445	9.802	17.218	0.076	0.001	0.001	0.192	0.474
91500-40	60	6.819	0.087	0.184	0.147	0.002	0.004	942.077	12.054	18.691	0.076	0.001	0.001	0.284	0.410
91500-41	60	6.848	0.097	0.187	0.146	0.002	0.004	920.675	11.346	17.725	0.074	0.001	0.002	0.399	0.403
91500-42	60	6.839	0.088	0.182	0.147	0.002	0.004	926.371	12.669	18.626	0.074	0.001	0.001	0.203	0.470
91500-43	60	6.871	0.092	0.184	0.146	0.002	0.004	926.338	12.069	18.330	0.074	0.001	0.001	0.238	0.435
91500-44	60	6.963	0.096	0.191	0.144	0.002	0.004	920.122	11.109	17.786	0.075	0.001	0.002	0.375	0.364
91500-45	60	6.910	0.100	0.191	0.145	0.002	0.004	933.534	14.385	19.921	0.076	0.002	0.002	0.290	0.366
91500-46	60	6.762	0.077	0.174	0.148	0.002	0.004	950.442	12.767	18.542	0.077	0.002	0.002	0.287	0.292
91500-47	60	6.731	0.083	0.181	0.149	0.002	0.004	939.857	12.758	18.705	0.074	0.001	0.002	0.139	0.450
91500-48	60	6.836	0.089	0.185	0.146	0.002	0.004	930.182	13.709	19.295	0.075	0.002	0.002	0.224	0.374
91500-49	60	6.649	0.088	0.178	0.151	0.002	0.004	950.330	13.426	19.397	0.075	0.002	0.002	0.314	0.325
91500-5	60	6.597	0.066	0.169	0.152	0.002	0.004	968.114	9.145	16.646	0.076	0.001	0.001	0.234	0.450
91500-50	60	6.760	0.088	0.184	0.148	0.002	0.004	939.048	15.230	20.689	0.075	0.002	0.002	0.220	0.365
91500-51	60	6.892	0.092	0.186	0.145	0.002	0.004	921.223	14.073	19.527	0.074	0.002	0.002	0.299	0.306
91500-52	60	7.063	0.097	0.203	0.142	0.002	0.004	903.538	14.478	20.023	0.073	0.002	0.002	0.263	0.352
91500-53	60	7.008	0.094	0.194	0.143	0.002	0.004	909.294	13.775	19.287	0.074	0.002	0.002	0.174	0.481
91500-54	60	6.965	0.077	0.182	0.144	0.002	0.004	919.837	13.822	19.352	0.075	0.002	0.002	0.275	0.238
91500-55	60	6.963	0.075	0.181	0.144	0.002	0.004	925.675	13.777	19.393	0.075	0.002	0.002	0.161	0.352
91500-6	60	6.594	0.062	0.170	0.152	0.001	0.004	951.873	11.121	18.091	0.074	0.001	0.001	0.198	0.361
91500-7	60	6.574	0.069	0.172	0.152	0.002	0.004	952.837	11.151	17.726	0.074	0.001	0.001	0.035	0.578
91500-8	60	6.543	0.069	0.170	0.153	0.002	0.004	956.785	9.730	16.943	0.074	0.001	0.001	0.155	0.550
91500-9	60	6.548	0.069	0.164	0.153	0.002	0.004	958.597	11.512	18.130	0.075	0.001	0.001	0.121	0.518
RAK-17- Zircon															
RAK-1	30	23.541	0.254	0.716	0.043	0.000	0.001	0.307	0.005	0.010	0.052	0.001	0.001	0.137	0.456
RAK-10	30	22.833	0.257	0.711	0.044	0.000	0.001	0.317	0.006	0.011	0.052	0.001	0.001	0.239	0.325
RAK-11	30	22.800	0.248	0.703	0.044	0.000	0.001	0.315	0.007	0.011	0.052	0.001	0.001	0.166	0.360
RAK-12	30	23.901	0.279	0.734	0.042	0.000	0.001	0.303	0.006	0.011	0.052	0.001	0.001	0.132	0.445
RAK-13	30	22.786	0.255	0.705	0.044	0.000	0.001	0.317	0.007	0.011	0.052	0.001	0.001	0.057	0.474
RAK-14	30	22.724	0.276	0.704	0.044	0.001	0.001	0.316	0.007	0.011	0.052	0.001	0.001	0.189	0.394
RAK-15	30	23.112	0.261	0.711	0.043	0.000	0.001	0.320	0.007	0.011	0.054	0.001	0.001	0.162	0.369
RAK-16	30	22.730	0.195	0.690	0.044	0.000	0.001	0.324	0.006	0.011	0.053	0.001	0.001	0.250	0.162
RAK-17	30	23.086	0.236	0.715	0.043	0.000	0.001	0.309	0.007	0.011	0.052	0.001	0.001	0.139	0.331

RAK-18	30	22.423	0.205	0.671	0.045	0.000	0.001	0.318	0.006	0.011	0.052	0.001	0.001	0.195	0.270
RAK-2	30	23.197	0.240	0.705	0.043	0.000	0.001	0.314	0.005	0.010	0.053	0.001	0.001	0.056	0.535
RAK-3	30	22.937	0.229	0.691	0.044	0.000	0.001	0.324	0.005	0.011	0.054	0.001	0.001	0.481	0.061
RAK-4	30	23.375	0.244	0.717	0.043	0.000	0.001	0.318	0.006	0.011	0.053	0.001	0.001	0.199	0.391
RAK-5	30	23.471	0.256	0.725	0.043	0.000	0.001	0.309	0.006	0.011	0.052	0.001	0.001	0.085	0.427
RAK-6	30	22.111	0.206	0.658	0.045	0.000	0.001	0.320	0.006	0.011	0.051	0.001	0.001	0.240	0.260
RAK-7	30	23.178	0.266	0.725	0.043	0.000	0.001	0.306	0.007	0.011	0.051	0.001	0.001	0.111	0.403
RAK-8	30	22.443	0.234	0.693	0.045	0.000	0.001	0.321	0.007	0.011	0.052	0.001	0.001	0.281	0.226
RAK-9	30	23.166	0.280	0.715	0.043	0.001	0.001	0.314	0.007	0.011	0.053	0.001	0.001	0.160	0.410
G_NIST610 (Day 1)															
NIST 610-1		5.073	0.052	0.152	0.198	0.002	0.006	24.712	0.265	0.748	0.907	0.003	0.004	0.065	0.948
NIST 610-10	30	4.969	0.049	0.147	0.202	0.002	0.006	25.144	0.256	0.756	0.904	0.003	0.004	0.188	0.921
NIST 610-11	30	5.037	0.044	0.148	0.199	0.002	0.006	24.811	0.232	0.742	0.907	0.003	0.004	0.014	0.929
NIST 610-12	30	5.131	0.047	0.151	0.195	0.002	0.006	24.328	0.225	0.724	0.905	0.003	0.004	0.225	0.932
NIST 610-13	30	4.924	0.050	0.146	0.204	0.002	0.006	25.312	0.262	0.762	0.902	0.005	0.005	0.252	0.836
NIST 610-14	30	5.155	0.050	0.156	0.194	0.002	0.006	24.293	0.253	0.734	0.907	0.005	0.005	0.237	0.862
NIST 610-15	30	5.066	0.052	0.151	0.198	0.002	0.006	24.715	0.246	0.742	0.907	0.004	0.005	0.358	0.871
NIST 610-16	30	5.078	0.049	0.151	0.198	0.002	0.006	24.635	0.235	0.735	0.906	0.004	0.005	0.268	0.901
NIST 610-17	30	4.939	0.050	0.147	0.203	0.002	0.006	25.379	0.257	0.763	0.907	0.004	0.005	0.278	0.892
NIST 610-19	30	5.022	0.044	0.149	0.199	0.002	0.006	24.983	0.223	0.739	0.909	0.004	0.005	0.298	0.830
NIST 610-2	30	5.268	0.058	0.157	0.191	0.002	0.006	23.864	0.277	0.729	0.908	0.003	0.004	0.112	0.947
NIST 610-3	30	5.183	0.049	0.154	0.194	0.002	0.006	24.134	0.228	0.719	0.905	0.003	0.004	0.204	0.935
NIST 610-4	30	5.060	0.055	0.151	0.199	0.002	0.006	24.676	0.269	0.749	0.903	0.003	0.004	0.204	0.947
NIST 610-5	30	5.169	0.049	0.156	0.194	0.002	0.006	24.253	0.227	0.722	0.907	0.003	0.004	0.246	0.942
NIST 610-6	30	4.916	0.049	0.144	0.204	0.002	0.006	25.387	0.266	0.767	0.902	0.004	0.005	0.185	0.913
NIST 610-7	30	5.034	0.048	0.149	0.199	0.002	0.006	24.920	0.239	0.744	0.909	0.004	0.004	0.211	0.912
NIST 610-8	30	5.064	0.054	0.151	0.198	0.002	0.006	24.744	0.264	0.749	0.907	0.003	0.004	0.239	0.954
NIST 610-9	30	5.096	0.050	0.154	0.197	0.002	0.006	24.543	0.243	0.735	0.906	0.004	0.004	0.198	0.917
G_NIST610 (Day 2)															
NIST 610 - 1		5.136	0.073	0.142	0.196	0.003	0.005	3288.027	13.013	25.248	0.912	0.010	0.012	0.505	0.709
NIST 610 - 10	60	5.122	0.057	0.130	0.196	0.002	0.005	3281.471	11.887	25.020	0.903	0.007	0.009	0.357	0.756
NIST 610 - 11	60	5.181	0.063	0.132	0.194	0.002	0.005	3272.510	13.090	25.175	0.907	0.007	0.010	0.263	0.791
NIST 610 - 12	60	5.126	0.069	0.137	0.196	0.003	0.005	3279.858	13.712	25.689	0.904	0.009	0.011	0.404	0.741
NIST 610 - 13	60	5.127	0.062	0.133	0.195	0.002	0.005	3279.596	12.308	25.027	0.905	0.009	0.011	0.453	0.691
NIST 610 - 14	60	5.180	0.076	0.141	0.194	0.003	0.005	3272.733	13.355	25.514	0.905	0.009	0.010	0.439	0.795
NIST 610 - 15	60	5.069	0.067	0.134	0.198	0.003	0.005	3295.539	12.532	25.047	0.908	0.009	0.010	0.487	0.734
NIST 610 - 16	60	5.139	0.071	0.143	0.195	0.003	0.005	3275.924	12.551	25.231	0.907	0.008	0.010	0.382	0.827
NIST 610 - 17	60	5.134	0.068	0.136	0.196	0.003	0.005	3287.455	13.697	25.705	0.913	0.010	0.012	0.441	0.682
NIST 610 - 18	60	5.189	0.065	0.135	0.193	0.002	0.005	3276.133	13.105	25.357	0.913	0.008	0.010	0.355	0.766
NIST 610 - 19	60	5.018	0.069	0.136	0.200	0.003	0.005	3301.397	14.187	25.892	0.903	0.009	0.011	0.406	0.738
NIST 610 - 2	60	4.918	0.065	0.132	0.204	0.003	0.006	3321.957	11.904	24.729	0.904	0.008	0.010	0.529	0.772
NIST 610 - 20	60	5.109	0.062	0.132	0.196	0.002	0.005	3292.331	13.709	26.885	0.913	0.008	0.010	0.202	0.816
NIST 610 - 21	60	4.919	0.072	0.137	0.204	0.003	0.006	3319.512	15.597	27.877	0.902	0.009	0.011	0.342	0.748
NIST 610 - 22	60	5.000	0.073	0.136	0.201	0.003	0.006	3307.141	14.977	26.732	0.907	0.010	0.012	0.377	0.693
NIST 610 - 23	60	5.073	0.070	0.143	0.197	0.003	0.005	3296.381	14.342	25.938	0.911	0.009	0.011	0.320	0.780
NIST 610 - 24	60	4.933	0.052	0.122	0.203	0.002	0.005	3321.379	10.405	23.933	0.908	0.004	0.007	0.365	0.865
NIST 610 - 25	60	4.885	0.059	0.128	0.205	0.003	0.005	3330.780	11.431	24.503	0.907	0.006	0.009	0.437	0.812
NIST 610 - 26	60	5.152	0.073	0.140	0.195	0.003	0.005	3282.947	13.255	25.285	0.910	0.009	0.011	0.486	0.786
NIST 610 - 27	60	5.335	0.081	0.147	0.189	0.003	0.005	3249.628	14.054	25.684	0.909	0.010	0.012	0.538	0.727
NIST 610 - 28	60	5.227	0.080	0.148	0.192	0.003	0.005	3265.706	13.434	25.255	0.909	0.009	0.011	0.545	0.788
NIST 610 - 3	60	4.931	0.059	0.128	0.203	0.003	0.005	3330.195	12.567	24.849	0.913	0.005	0.008	0.264	0.875
NIST 610 - 4	60	4.927	0.073	0.142	0.204	0.003	0.006	3327.016	12.627	25.778	0.908	0.007	0.010	0.554	0.821
NIST 610 - 5	60	4.999	0.055	0.125	0.201	0.002	0.005	3315.800	11.507	24.446	0.914	0.004	0.008	0.322	0.895
NIST 610 - 6	60	5.048	0.078	0.143	0.199	0.003	0.006	3291.903	15.411	26.917	0.902	0.011	0.012	0.379	0.709
NIST 610 - 7	60	5.251	0.078	0.143	0.191	0.003	0.005	3258.734	14.626	26.521	0.904	0.010	0.012	0.457	0.746
NIST 610 - 8	60	5.225	0.082	0.147	0.193	0.003	0.005	3266.103	15.731	27.036	0.909	0.010	0.012	0.385	0.744
NIST 610 - 9	60	5.290	0.080	0.146	0.190	0.003	0.005	3253.756	13.344	25.348	0.908	0.009	0.011	0.560	0.740
Hematite Unknowns															
Fe-Grab															
Fe-Grab-1	60	0.23	0.01	0.01	4.64	0.17	0.22	371.68	16.42	19.50	0.59	0.01	0.01	-0.08	0.88
Fe-Grab-10	60	1.84	0.18	0.19	0.81	0.09	0.09	70.65	9.24	9.45	0.65	0.05	0.05	0.13	0.85
Fe-Grab-11	60	1.37	0.11	0.12	0.92	0.08	0.08	78.73	7.08	7.43	0.64	0.03	0.03	0.06	0.10
Fe-Grab-12	60	1.54	0.11	0.12	0.77	0.06	0.06	70.91	5.70	6.05	0.70	0.05	0.05	0.48	0.46
Fe-Grab-13	60	0.96	0.05	0.06	1.15	0.08	0.08	99.20	7.27	7.79	0.63	0.03	0.03	0.27	0.82
Fe-Grab-14	60	2.13	0.18	0.19	0.59	0.05	0.05	44.08	4.43	4.60	0.56	0.04	0.04	0.44	0.82
Fe-Grab-15	60	1.60	0.12	0.12	0.78	0.07	0.08	64.60	7.50	7.72	0.60	0.03	0.03	0.08	0.93
Fe-Grab-16	60	1.74	0.15	0.16	0.78	0.07	0.07	70.53	7.44	7.70	0.64	0.03	0.03	-0.03	0.90
Fe-Grab-17	60	1.95	0.13	0.14	0.60	0.05	0.05	49.38	4.19	4.42	0.61	0.04	0.04	0.43	0.80
Fe-Grab-18	60	3.79	0.42	0.44	0.39	0.04	0.04	30.35	7.53	7.58	0.58	0.07	0.07	0.01	0.82
Fe-Grab-19	60	6.59	0.80	0.81	0.38	0.06	0.06	27.51	6.13	6.18	0.37	0.05	0.05	0.45	0.94
Fe-Grab-2	60	2.58	0.15	0.17	0.44	0.03	0.03	35.87	4.36	4.48	0.58	0.04	0.04	0.00	0.24
Fe-Grab-20	60	9.83	1.03	1.04	0.19	0.04	0.04	15.48	4.77	4.79	0.43	0.07	0.07	0.15	0.70
Fe-Grab-21	60	2.81	0.17	0.19	0.41	0.03	0.03	29.81	2.85	2.97	0.54	0.03	0.03	0.02	0.83
Fe-Grab-22	60	5.57	0.47	0.49	0.23	0.02	0.02	17.68	2.67	2.72	0.49	0.04	0.04	0.41	0.89
Fe-Grab-23	60	1.76	0.11	0.12	0.67	0.05	0.06	53.75	4.10	4.37	0.63	0.04	0.04	0.17	0.27
Fe-Grab-24	60	3.47	0.27	0.28	0.36	0.04	0.04	27.70	3.28	3.38	0.62	0.06	0.06	0.65	0.90
Fe-Grab-25	60	2.28	0.17	0.19	0.52	0.04	0.04	43.33	4.80	4.95	0.59	0.03	0.03	0.11	0.98
Fe-Grab-26	60	2.17	0.14	0.15	0.53	0.04	0.04	42.18	3.49	3.69	0.60	0.03	0.03	0.24	0.64
Fe-Grab-27	60	5.35	0.29	0.32	0.21	0.01	0.02	12.67	1.25	1.30	0.44	0.03	0.03	-0.04	0.78

Fe-Grab-28	60	2.06	0.14	0.15	0.57	0.04	0.04	45.19	3.69	3.90	0.58	0.04	0.04	0.31	0.67
Fe-Grab-29	60	5.43	0.53	0.55	0.25	0.02	0.03	16.73	2.12	2.17	0.52	0.05	0.05	0.74	0.74
Fe-Grab-3	60	1.95	0.18	0.19	0.72	0.06	0.07	56.03	5.60	5.82	0.55	0.03	0.03	0.10	0.48
Fe-Grab-30	60	8.74	0.50	0.56	0.13	0.01	0.01	5.42	1.26	1.27	0.26	0.05	0.05	-0.04	0.39
Fe-Grab-31	60	1.08	0.15	0.15	1.87	0.28	0.29	187.89	31.15	31.60	0.80	0.08	0.08	0.33	0.89
Fe-Grab-32	60	3.64	0.88	0.88	1.20	0.33	0.33	82.78	27.77	27.87	0.53	0.12	0.12	0.27	0.88
Fe-Grab-33	60	10.02	0.59	0.64	0.11	0.01	0.01	3.93	0.89	0.90	0.20	0.03	0.03	-0.31	0.83
Fe-Grab-34	60	1.82	0.17	0.17	0.72	0.06	0.07	65.92	5.49	5.80	0.75	0.06	0.06	0.24	0.50
Fe-Grab-35	60	2.28	0.19	0.21	0.55	0.04	0.04	45.67	3.81	4.02	0.59	0.03	0.03	0.00	0.78
Fe-Grab-36	60	3.59	0.28	0.29	0.35	0.03	0.03	28.58	2.96	3.07	0.60	0.04	0.04	0.20	0.82
Fe-Grab-37	60	4.73	0.55	0.57	0.35	0.05	0.05	25.55	4.55	4.60	0.57	0.07	0.07	0.83	0.93
Fe-Grab-38	60	7.48	0.44	0.47	0.15	0.01	0.01	7.22	0.94	0.96	0.36	0.03	0.03	0.17	0.89
Fe-Grab-39	60	1.32	0.12	0.12	0.99	0.08	0.09	86.83	8.77	9.11	0.68	0.05	0.05	0.25	0.68
Fe-Grab-4	60	1.99	0.25	0.25	0.90	0.14	0.14	87.21	17.16	17.34	0.67	0.06	0.06	0.36	0.97
Fe-Grab-40	60	3.93	0.27	0.29	0.31	0.02	0.02	19.85	1.87	1.95	0.45	0.03	0.03	-0.19	0.69
Fe-Grab-41	60	2.64	0.24	0.26	0.50	0.04	0.04	39.56	3.95	4.10	0.58	0.03	0.03	0.20	0.76
Fe-Grab-42	60	2.90	0.39	0.40	0.59	0.09	0.09	52.20	11.54	11.64	0.62	0.07	0.07	0.58	0.87
Fe-Grab-43	60	8.37	1.28	1.28	0.40	0.12	0.12	33.50	14.54	14.57	0.51	0.08	0.08	0.58	0.99
Fe-Grab-44	60	3.55	0.30	0.31	0.39	0.04	0.05	31.33	4.86	4.94	0.59	0.05	0.05	0.21	0.73
Fe-Grab-45	60	4.24	0.49	0.49	0.44	0.09	0.09	39.72	9.58	9.64	0.64	0.07	0.07	0.47	0.92
Fe-Grab-46	60	3.29	0.23	0.26	0.36	0.02	0.03	29.52	2.72	2.84	0.62	0.05	0.05	0.39	0.61
Fe-Grab-47	60	2.79	0.22	0.23	0.51	0.07	0.07	44.49	7.19	7.30	0.59	0.03	0.03	0.14	0.96
Fe-Grab-5	60	2.77	0.19	0.20	0.45	0.04	0.04	32.18	3.04	3.18	0.53	0.03	0.03	0.18	0.92
Fe-Grab-6	60	3.27	0.28	0.29	0.40	0.04	0.04	36.35	4.29	4.41	0.70	0.07	0.07	0.57	0.78
Fe-Grab-7	60	1.60	0.09	0.10	0.72	0.05	0.05	51.91	3.42	3.72	0.56	0.03	0.03	0.26	0.47
Fe-Grab-8	60	2.47	0.26	0.26	0.92	0.23	0.23	74.89	21.83	21.94	0.59	0.05	0.05	0.34	0.95
Fe-Grab-9	60	3.27	0.20	0.22	0.34	0.02	0.02	23.21	2.12	2.22	0.52	0.04	0.04	0.22	0.86
JK_21 Band															
JK_21_G_Band-1	60	1.18	0.11	0.11	1.02	0.07	0.08	110.44	9.48	9.98	0.74	0.02	0.02	-0.24	0.97
JK_21_G_Band-10	60	1.32	0.06	0.07	0.80	0.04	0.05	70.27	3.84	4.32	0.64	0.02	0.02	-0.03	0.91
JK_21_G_Band-11	60	1.09	0.04	0.05	0.96	0.04	0.05	92.04	4.38	5.10	0.70	0.02	0.02	0.20	0.83
JK_21_G_Band-12	60	0.92	0.04	0.05	1.16	0.05	0.06	117.80	6.90	7.67	0.73	0.02	0.02	0.01	0.58
JK_21_G_Band-13	60	1.11	0.05	0.05	0.97	0.05	0.06	87.83	4.76	5.37	0.67	0.02	0.02	0.33	0.86
JK_21_G_Band-14	60	1.06	0.05	0.05	1.00	0.04	0.05	93.95	4.30	5.05	0.69	0.02	0.02	0.24	0.87
JK_21_G_Band-15	60	1.01	0.04	0.05	1.04	0.05	0.06	100.79	4.94	5.71	0.71	0.02	0.02	0.34	0.87
JK_21_G_Band-16	60	1.07	0.04	0.05	0.96	0.03	0.04	91.91	3.76	4.57	0.69	0.02	0.02	0.21	0.76
JK_21_G_Band-17	60	1.20	0.08	0.08	0.96	0.06	0.07	91.10	6.54	7.03	0.67	0.02	0.02	-0.16	0.90
JK_21_G_Band-18	60	1.16	0.05	0.06	0.91	0.04	0.05	84.44	4.07	4.72	0.68	0.02	0.02	0.26	0.87
JK_21_G_Band-19	60	0.82	0.05	0.06	1.48	0.11	0.12	154.40	12.48	13.23	0.75	0.02	0.02	-0.04	0.85
JK_21_G_Band-2	60	0.88	0.04	0.05	1.22	0.07	0.08	125.17	7.41	8.22	0.76	0.02	0.02	0.08	0.95
JK_21_G_Band-20	60	0.84	0.05	0.05	1.37	0.11	0.12	144.79	12.93	13.57	0.75	0.02	0.02	-0.02	0.91
JK_21_G_Band-21	60	1.06	0.05	0.06	1.03	0.06	0.07	99.71	6.67	7.24	0.70	0.02	0.02	0.23	0.92
JK_21_G_Band-22	60	1.12	0.05	0.06	0.94	0.05	0.05	87.40	4.47	5.11	0.69	0.02	0.02	0.16	0.66
JK_21_G_Band-23	60	1.06	0.04	0.05	0.98	0.04	0.05	94.49	4.30	5.07	0.72	0.02	0.02	0.20	0.84
JK_21_G_Band-24	60	1.12	0.05	0.06	0.98	0.06	0.06	93.33	5.51	6.11	0.71	0.02	0.02	0.18	0.65
JK_21_G_Band-25	60	1.19	0.05	0.06	0.89	0.04	0.05	82.15	4.03	4.66	0.68	0.02	0.02	0.27	0.87
JK_21_G_Band-26	60	1.14	0.05	0.06	0.94	0.05	0.06	88.04	5.80	6.32	0.68	0.02	0.02	0.15	0.82
JK_21_G_Band-27	60	1.03	0.05	0.05	1.02	0.05	0.06	104.67	5.99	6.69	0.75	0.03	0.03	0.30	0.89
JK_21_G_Band-28	60	1.08	0.05	0.05	1.01	0.06	0.06	93.84	5.32	5.94	0.69	0.02	0.02	0.18	0.91
JK_21_G_Band-29	60	1.50	0.06	0.07	0.68	0.03	0.03	61.72	2.62	3.15	0.65	0.02	0.02	0.35	0.66
JK_21_G_Band-3	60	1.09	0.05	0.06	0.93	0.04	0.04	90.01	4.22	4.93	0.70	0.02	0.02	0.16	0.93
JK_21_G_Band-30	60	1.51	0.05	0.07	0.70	0.03	0.03	62.01	2.66	3.19	0.65	0.02	0.02	0.09	0.07
JK_21_G_Band-31	60	1.57	0.05	0.07	0.66	0.02	0.03	55.20	2.06	2.59	0.62	0.02	0.02	0.19	0.80
JK_21_G_Band-32	60	1.35	0.04	0.06	0.77	0.03	0.03	67.73	2.01	2.78	0.66	0.02	0.02	0.47	0.47
JK_21_G_Band-33	60	1.09	0.06	0.07	1.03	0.06	0.07	103.28	6.78	7.38	0.75	0.04	0.04	0.08	0.20
JK_21_G_Band-34	60	1.53	0.06	0.08	0.68	0.03	0.03	58.79	2.83	3.28	0.63	0.02	0.02	0.09	0.17
JK_21_G_Band-35	60	1.69	0.06	0.08	0.61	0.02	0.03	53.26	2.38	2.82	0.63	0.02	0.02	0.30	0.82
JK_21_G_Band-36	60	1.62	0.06	0.08	0.64	0.02	0.03	52.95	2.42	2.84	0.60	0.02	0.02	0.12	0.83
JK_21_G_Band-37	60	1.41	0.06	0.07	0.74	0.03	0.04	66.87	2.80	3.38	0.67	0.02	0.02	0.37	0.84
JK_21_G_Band-38	60	1.41	0.05	0.06	0.73	0.03	0.03	65.39	2.68	3.26	0.66	0.02	0.02	0.09	0.86
JK_21_G_Band-39	60	1.42	0.06	0.07	0.75	0.04	0.05	64.98	4.02	4.42	0.65	0.02	0.02	0.04	0.70
JK_21_G_Band-4	60	1.11	0.04	0.05	0.93	0.04	0.05	89.60	4.08	4.81	0.70	0.02	0.02	0.30	0.91
JK_21_G_Band-40	60	1.43	0.07	0.08	0.76	0.04	0.05	64.72	4.36	4.73	0.63	0.03	0.03	0.22	0.84
JK_21_G_Band-41	60	1.13	0.06	0.07	1.00	0.05	0.06	100.68	6.37	6.98	0.72	0.02	0.02	-0.18	0.93
JK_21_G_Band-42	60	1.58	0.10	0.13	0.67	0.03	0.04	60.49	3.41	3.82	0.64	0.02	0.02	-0.01	0.67
JK_21_G_Band-43	60	1.51	0.06	0.07	0.71	0.03	0.04	59.49	2.87	3.32	0.63	0.02	0.02	0.28	0.55
JK_21_G_Band-44	60	1.01	0.07	0.08	1.17	0.08	0.09	122.05	9.29	9.91	0.74	0.02	0.02	-0.05	0.92
JK_21_G_Band-45	60	1.26	0.05	0.06	0.83	0.04	0.04	75.36	3.89	4.43	0.66	0.02	0.02	0.06	0.50
JK_21_G_Band-46	60	1.56	0.06	0.07	0.66	0.03	0.03	56.56	2.70	3.14	0.63	0.02	0.02	0.29	0.81
JK_21_G_Band-47	60	1.88	0.08	0.09	0.56	0.03	0.03	44.32	2.21	2.54	0.60	0.02	0.02	0.22	0.82
JK_21_G_Band-48	60	1.77	0.08	0.09	0.59	0.03	0.03	51.27	3.09	3.41	0.62	0.02	0.02	0.19	0.89
JK_21_G_Band-49	60	1.69	0.10	0.11	0.68	0.05	0.05	56.33	4.16	4.46	0.62	0.02	0.02	0.14	0.73
JK_21_G_Band-5	60	1.27	0.05	0.06	0.83	0.04	0.04	72.94	3.49	4.06	0.66	0.02	0.02	0.17	0.86
JK_21_G_Band-50	60	1.55	0.07	0.08	0.68	0.03	0.04	58.43	3.34	3.72	0.63	0.02	0.02	0.24	0.85
JK_21_G_Band-51	60	1.45	0.06	0.07	0.72	0.03	0.04	62.51	3.04	3.51	0.65	0.02	0.02	0.16	0.66
JK_21_G_Band-52	60	1.98	0.06	0.09	0.52	0.02	0.02	37.59	1.38	1.74	0.54	0.02	0.02	0.18	0.75
JK_21_G_Band-53	60	1.63	0.08	0.09	0.67	0.04	0.04	50.90	2.73	3.09	0.58	0.02	0.02	0.36	0.41
JK_21_G_Band-54	60	1.64	0.09	0.09	0.69	0.05	0.05	52.84	3.03	3.38	0.60	0.02	0.02	0.18	0.27
JK_21_G_Band-55	60	1.79	0.07	0.09	0.58	0.03	0.03	52.05	3.13	3.46	0.66	0.04	0.04	0.10	0.18

JK_21_G_Band-56	60	1.59	0.05	0.08	0.65	0.02	0.03	56.61	1.97	2.54	0.63	0.02	0.02	0.10	0.61
JK_21_G_Band-57	60	1.60	0.07	0.08	0.67	0.03	0.04	58.47	3.39	3.77	0.63	0.02	0.02	0.10	0.85
JK_21_G_Band-58	60	1.46	0.06	0.07	0.71	0.03	0.04	58.18	2.71	3.17	0.60	0.02	0.02	0.23	0.85
JK_21_G_Band-59	60	1.28	0.04	0.05	0.81	0.03	0.04	73.90	3.29	3.90	0.68	0.02	0.02	0.17	0.64
JK_21_G_Band-6	60	1.17	0.05	0.06	0.91	0.05	0.06	85.04	4.73	5.30	0.69	0.02	0.02	0.13	0.96
JK_21_G_Band-60	60	1.45	0.05	0.07	0.71	0.03	0.03	59.17	2.13	2.71	0.62	0.02	0.02	0.44	0.85
JK_21_G_Band-7	60	1.13	0.05	0.06	0.96	0.06	0.06	92.43	6.63	7.13	0.69	0.02	0.02	0.04	0.85
JK_21_G_Band-8	60	1.19	0.06	0.06	0.91	0.05	0.06	85.72	4.90	5.47	0.69	0.02	0.02	0.14	0.93
JK_21_G_Band-9	60	1.30	0.05	0.06	0.80	0.03	0.04	71.28	2.94	3.56	0.66	0.02	0.02	0.20	0.88
JK_21 Vein															
JK_21_G_Vein-1	60	0.009	0.003	0.003	-322.823	65.241	65.897	-42941.906	8624.883	8710.144	0.973	0.023	0.024	0.115	0.795
JK_21_G_Vein-10	60	0.112	0.006	0.006	10.089	0.574	0.643	1282.012	74.048	82.467	0.923	0.007	0.008	-0.020	0.989
JK_21_G_Vein-11	60	0.222	0.007	0.010	4.687	0.147	0.199	580.205	18.499	24.741	0.902	0.013	0.013	0.068	0.720
JK_21_G_Vein-12	60	0.210	0.006	0.009	4.896	0.148	0.204	620.244	19.166	25.994	0.921	0.011	0.011	0.127	0.928
JK_21_G_Vein-13	60	0.273	0.032	0.035	4.572	0.320	0.346	548.653	38.016	41.067	0.899	0.036	0.037	0.119	0.483
JK_21_G_Vein-14	60	0.085	0.006	0.007	14.044	0.818	0.912	1797.318	105.174	116.839	0.931	0.008	0.008	-0.128	0.990
JK_21_G_Vein-15	60	0.127	0.004	0.005	8.041	0.244	0.336	1028.115	29.485	41.435	0.927	0.009	0.009	0.193	0.959
JK_21_G_Vein-16	60	0.460	0.049	0.052	3.168	0.256	0.272	401.316	34.884	36.687	0.890	0.017	0.017	-0.189	0.969
JK_21_G_Vein-17	60	0.246	0.013	0.016	4.316	0.192	0.228	529.828	23.909	28.226	0.892	0.016	0.016	0.057	0.919
JK_21_G_Vein-18	60	0.514	0.038	0.041	2.483	0.180	0.194	300.418	22.497	24.051	0.882	0.019	0.019	0.075	0.959
JK_21_G_Vein-19	60	0.205	0.008	0.009	5.175	0.215	0.261	641.943	26.267	31.941	0.914	0.015	0.015	0.171	0.898
JK_21_G_Vein-2	60	0.078	0.009	0.009	13.439	5.198	5.213	1214.169	945.590	946.214	0.921	0.029	0.029	-0.140	0.981
JK_21_G_Vein-20	60	0.113	0.014	0.015	14.723	1.318	1.384	1893.714	174.037	182.106	0.929	0.013	0.013	0.022	0.989
JK_21_G_Vein-21	60	0.027	0.003	0.003	69.728	9.557	9.765	9001.154	1239.518	1265.445	0.937	0.013	0.013	-0.017	0.992
JK_21_G_Vein-22	60	0.140	0.012	0.013	10.117	1.072	1.110	1293.803	138.485	143.248	0.923	0.012	0.012	-0.111	0.996
JK_21_G_Vein-23	60	0.285	0.012	0.014	3.745	0.150	0.184	459.438	18.096	22.284	0.898	0.014	0.014	0.126	0.912
JK_21_G_Vein-24	60	0.519	0.080	0.081	6.832	1.501	1.514	869.332	201.879	203.374	0.878	0.041	0.041	0.127	0.965
JK_21_G_Vein-25	60	0.536	0.057	0.059	2.617	0.253	0.264	299.581	29.532	30.725	0.837	0.035	0.035	0.038	0.545
JK_21_G_Vein-26	60	0.104	0.013	0.013	18.737	2.720	2.772	2447.390	370.271	376.697	0.949	0.022	0.022	0.011	1.000
JK_21_G_Vein-27	60	0.204	0.013	0.014	6.049	0.547	0.574	747.770	66.554	69.840	0.925	0.021	0.021	-0.019	0.964
JK_21_G_Vein-28	60	0.246	0.013	0.015	4.435	0.258	0.288	564.269	34.128	37.682	0.912	0.023	0.023	0.014	0.919
JK_21_G_Vein-29	60	0.117	0.011	0.012	12.764	1.388	1.436	1636.287	183.022	188.792	0.936	0.026	0.026	0.128	0.977
JK_21_G_Vein-3	60	0.091	0.007	0.007	14.581	1.526	1.582	1859.142	189.001	196.194	0.936	0.021	0.021	0.003	0.991
JK_21_G_Vein-30	60	0.216	0.010	0.011	5.030	0.252	0.291	637.386	34.515	38.947	0.920	0.021	0.021	0.013	0.428
JK_21_G_Vein-31	60	0.138	0.008	0.009	8.192	0.485	0.539	1040.036	63.290	69.802	0.929	0.017	0.017	0.113	0.960
JK_21_G_Vein-32	60	0.116	0.008	0.009	10.031	0.667	0.727	1300.359	90.239	97.458	0.938	0.016	0.016	0.133	0.966
JK_21_G_Vein-33	60	0.147	0.005	0.006	7.051	0.254	0.325	889.636	33.134	41.617	0.922	0.014	0.015	0.106	0.915
JK_21_G_Vein-34	60	0.194	0.005	0.007	5.298	0.136	0.204	662.926	15.192	24.145	0.919	0.013	0.013	0.231	0.867
JK_21_G_Vein-35	60	0.234	0.010	0.012	4.584	0.180	0.223	568.591	21.961	27.226	0.903	0.012	0.012	0.218	0.944
JK_21_G_Vein-36	60	0.640	0.046	0.049	1.912	0.133	0.144	227.371	17.072	18.245	0.844	0.018	0.018	-0.325	0.933
JK_21_G_Vein-37	60	0.156	0.014	0.014	8.732	0.851	0.887	1086.100	102.541	107.053	0.911	0.020	0.020	0.079	0.999
JK_21_G_Vein-38	60	0.197	0.033	0.036	7.166	0.440	0.486	916.569	56.431	62.111	0.926	0.019	0.019	-0.275	0.941
JK_21_G_Vein-39	60	0.117	0.006	0.006	9.324	0.499	0.566	1199.729	66.912	75.039	0.932	0.013	0.013	0.116	0.973
JK_21_G_Vein-4	60	0.103	0.005	0.006	10.497	0.527	0.607	1340.364	65.825	75.977	0.931	0.011	0.012	0.240	0.972
JK_21_G_Vein-40	60	0.095	0.005	0.006	11.877	0.642	0.727	1516.512	81.209	91.860	0.931	0.008	0.008	0.007	0.988
JK_21_G_Vein-41	60	0.312	0.014	0.016	3.438	0.156	0.185	429.331	19.887	23.307	0.914	0.012	0.012	0.066	0.955
JK_21_G_Vein-42	60	0.387	0.085	0.086	6.624	1.185	1.200	868.668	132.859	135.116	0.973	0.091	0.091	0.617	0.904
JK_21_G_Vein-43	60	0.203	0.033	0.033	4.915	2.415	2.419	586.945	309.307	309.753	0.985	0.077	0.077	0.066	0.884
JK_21_G_Vein-44	60	0.439	0.051	0.054	3.378	0.257	0.275	405.620	31.689	33.706	0.872	0.015	0.016	-0.221	0.970
JK_21_G_Vein-45	60	0.173	0.005	0.007	6.006	0.183	0.251	753.634	24.093	32.181	0.914	0.014	0.014	0.259	0.584
JK_21_G_Vein-5	60	0.150	0.038	0.038	-11.712	5.194	5.205	-1641.033	674.765	676.363	1.106	0.140	0.140	-0.024	0.721
JK_21_G_Vein-6	60	0.179	0.010	0.011	6.190	0.340	0.384	786.188	45.383	50.547	0.927	0.024	0.024	0.092	0.846
JK_21_G_Vein-7	60	0.144	0.009	0.010	7.992	0.466	0.520	1026.119	60.293	66.927	0.937	0.018	0.018	0.113	0.896
JK_21_G_Vein-8	60	0.285	0.012	0.015	3.690	0.152	0.185	456.766	20.602	24.325	0.892	0.014	0.014	0.034	0.932
JK_21_G_Vein-9	60	0.128	0.005	0.006	8.163	0.312	0.390	1035.451	40.691	50.149	0.918	0.013	0.014	0.119	0.931
JK23															
JK23_1	60	1.456	0.138	0.140	0.898	0.114	0.116	4244.444	133.003	134.184	0.633	0.043	0.043	0.167	0.584
JK23_10	60	1.604	0.126	0.132	0.689	0.054	0.056	4154.827	77.563	81.052	0.676	0.046	0.046	0.637	0.526
JK23_11	60	1.401	0.072	0.079	0.752	0.038	0.042	4453.862	56.984	61.651	0.812	0.033	0.033	0.265	0.768
JK23_12	60	4.872	0.375	0.389	0.243	0.021	0.021	2722.802	98.137	100.500	0.491	0.047	0.047	0.344	0.377
JK23_13	60	0.960	0.126	0.127	1.854	0.264	0.267	4877.562	154.589	155.907	0.716	0.058	0.058	0.244	1.000
JK23_14	60	6.280	0.403	0.416	0.179	0.016	0.017	2337.621	97.871	99.418	0.459	0.042	0.043	0.347	0.925
JK23_15	60	0.776	0.091	0.092	2.138	0.391	0.394	5129.130	136.164	137.386	0.758	0.041	0.042	-0.038	0.999
JK23_16	60	1.249	0.109	0.113	1.004	0.095	0.098	4499.564	100.951	103.685	0.704	0.042	0.043	0.434	0.879
JK23_18	60	5.504	0.339	0.362	0.199	0.013	0.013	2376.598	98.915	101.434	0.390	0.034	0.034	0.179	0.794
JK23_19	60	8.839	0.561	0.597	0.118	0.008	0.008	1235.445	96.198	97.664	0.158	0.022	0.022	0.482	0.143
JK23_2	60	3.765	0.256	0.267	0.306	0.025	0.026	3200.666	97.100	99.126	0.613	0.040	0.040	0.296	0.946
JK23_20	60	0.495	0.060	0.061	3.239	0.456	0.462	5585.794	140.762	142.368	0.774	0.053	0.053	0.018	0.807
JK23_21	60	4.658	0.274	0.293	0.239	0.015	0.016	2706.309	68.375	72.177	0.449	0.029	0.029	0.360	0.573
JK23_22	60	8.134	0.196	0.279	0.125	0.003	0.004	1651.805	36.070	40.730	0.247	0.012	0.012	0.421	0.149
JK23_23	60	0.464	0.024	0.027	2.283	0.113	0.125	5556.394	57.410	61.827	0.793	0.033	0.033	0.397	0.746
JK23_24	60	3.669	0.152	0.174	0.282	0.012	0.014	2849.753	62.001	66.141	0.423	0.023	0.023	0.291	0.650
JK23_25	60	1.595	0.099	0.106	0.680	0.040	0.044	4240.826	69.316	73.000	0.744	0.048	0.048	0.580	0.626
JK23_26	60	1.838	0.235	0.242	0.740	0.070	0.072	4169.842	134.513	137.677	0.692	0.061	0.061	0.043	0.726
JK23_27	60	0.284	0.031	0.031	5.170	0.599	0.612	6253.668	121.074	123.272	0.813	0.034	0.035	0.208	0.936
JK23_28	60	2.380	0.180	0.190	0.485	0.034	0.036	3660.438	85.001	88.715	0.607	0.034	0.034	0.236	0.705
JK23_29	60	2.794	0.151	0.167	0.386	0.019	0.021	3504.846	61.888	65.974	0.619	0.033	0.033	0.328	0.599
JK23_30	60	4.074	0.382	0.394	0.261	0.025	0.025	2916.558	165.617	167.290	0.511	0.071	0.071	0.089	0.597
JK23_31	60	6.414	0.214	0.256	0.160	0.006	0.007	1942.304	56.286	59.960	0.272	0.014	0.014	0.008	0.566

JK23_32	60	0.544	0.059	0.061	2.514	0.291	0.297	5445.066	121.553	123.387	0.764	0.052	0.052	0.105	0.762
JK23_33	60	0.952	0.067	0.070	1.209	0.087	0.092	4769.842	77.096	80.073	0.736	0.037	0.038	0.175	0.718
JK23_34	60	0.573	0.017	0.021	1.788	0.054	0.069	5240.935	32.707	40.103	0.721	0.016	0.017	0.264	0.739
JK23_35	60	4.342	0.492	0.506	0.277	0.027	0.028	2828.512	142.037	143.583	0.469	0.045	0.045	0.075	0.678
JK23_37	60	1.280	0.105	0.109	0.902	0.071	0.074	4441.235	109.524	112.818	0.704	0.040	0.040	-0.134	0.870
JK23_39	60	0.638	0.042	0.044	1.827	0.147	0.153	5158.666	72.031	75.626	0.718	0.034	0.035	0.334	0.860
JK23_4	60	0.626	0.094	0.095	4.213	1.176	1.180	5526.711	207.921	208.605	0.735	0.033	0.033	-0.126	0.992
JK23_40	60	0.464	0.038	0.039	2.686	0.234	0.243	5695.587	82.352	84.969	0.849	0.054	0.054	0.381	0.803
JK23_41	60	1.525	0.214	0.217	1.129	0.145	0.148	4347.733	189.048	191.247	0.643	0.049	0.049	-0.441	0.894
JK23_42	60	8.619	0.676	0.712	0.133	0.010	0.010	1773.286	140.597	142.732	0.325	0.038	0.038	-0.046	0.766
JK23_43	60	2.425	0.261	0.265	0.620	0.089	0.090	3706.960	163.524	164.573	0.627	0.057	0.057	0.243	0.947
JK23_44	60	8.008	0.277	0.335	0.128	0.004	0.005	1705.900	59.861	62.720	0.265	0.018	0.018	0.000	0.491
JK23_45	60	1.303	0.105	0.111	0.897	0.061	0.064	4445.940	84.343	87.762	0.699	0.035	0.036	0.092	0.740
JK23_46	60	0.752	0.101	0.104	1.914	0.187	0.192	5182.688	121.045	123.592	0.751	0.032	0.032	0.024	0.918
JK23_47	60	7.239	0.242	0.298	0.142	0.005	0.006	1947.790	64.276	67.704	0.315	0.020	0.020	0.219	0.299
JK23_48	60	2.391	0.159	0.170	0.471	0.029	0.031	3648.728	68.331	71.753	0.590	0.030	0.030	0.218	0.703
JK23_49	60	1.086	0.087	0.090	1.128	0.104	0.107	4618.893	93.811	96.070	0.731	0.056	0.056	0.563	0.771
JK23_5	60	2.494	0.209	0.218	0.492	0.040	0.042	3453.940	101.894	104.535	0.495	0.034	0.034	0.021	0.721
JK23_50	60	0.145	0.011	0.011	8.261	0.671	0.698	6860.999	72.376	75.606	0.855	0.032	0.032	0.318	0.938
JK23_51	60	1.855	0.098	0.106	0.586	0.033	0.036	4147.343	61.933	65.748	0.782	0.040	0.040	0.392	0.650
JK23_52	60	1.595	0.160	0.160	1.343	0.404	0.405	4222.429	166.963	167.530	0.657	0.067	0.067	0.879	0.901
JK23_54	60	0.534	0.044	0.045	2.249	0.190	0.197	5474.982	88.530	91.042	0.837	0.046	0.046	0.341	0.917
JK23_55	60	1.204	0.064	0.069	0.895	0.051	0.055	4396.815	74.879	78.354	0.658	0.025	0.025	-0.059	0.854
JK23_56	60	1.493	0.096	0.100	0.772	0.060	0.063	4109.440	87.220	89.763	0.567	0.021	0.021	0.006	0.928
JK23_57	60	1.618	0.104	0.112	0.693	0.043	0.046	4180.800	71.568	75.560	0.718	0.043	0.043	0.471	0.605
JK23_58	60	0.770	0.058	0.061	1.477	0.110	0.116	5180.738	75.819	78.847	0.911	0.057	0.057	0.499	0.814
JK23_59	60	1.247	0.076	0.082	0.891	0.053	0.057	4380.297	82.470	86.273	0.664	0.041	0.041	0.195	0.528
JK23_6	60	0.661	0.039	0.041	1.682	0.111	0.118	5157.065	65.835	69.631	0.747	0.031	0.031	0.254	0.808
JK23_60	60	3.144	0.165	0.180	0.344	0.019	0.020	3287.336	67.652	71.525	0.568	0.038	0.038	0.378	0.434
JK23_61	60	4.982	0.269	0.295	0.213	0.011	0.012	2571.943	72.717	75.916	0.429	0.030	0.030	0.661	0.564
JK23_62	60	3.424	0.306	0.320	0.348	0.028	0.029	3274.484	105.732	108.355	0.622	0.063	0.063	0.502	0.626
JK23_63	60	1.029	0.081	0.084	1.162	0.089	0.093	4701.483	85.103	88.261	0.733	0.043	0.044	0.419	0.728
JK23_64	60	0.780	0.077	0.079	1.732	0.184	0.188	5091.645	124.966	127.883	0.765	0.054	0.055	0.030	0.715
JK23_65	60	0.720	0.129	0.131	3.881	0.570	0.577	5776.788	193.965	196.163	0.876	0.031	0.032	-0.127	0.905
JK23_66	60	1.075	0.081	0.082	1.166	0.132	0.135	4610.464	122.854	124.151	0.638	0.029	0.029	-0.214	0.916
JK23_67	60	1.182	0.065	0.070	0.922	0.053	0.057	4684.059	69.241	72.986	0.847	0.047	0.048	0.409	0.543
JK23_68	60	3.007	0.374	0.384	0.490	0.051	0.052	3627.267	146.851	149.424	0.652	0.047	0.047	-0.164	0.798
JK23_69	60	0.700	0.042	0.045	1.580	0.103	0.109	5095.938	71.600	75.385	0.763	0.037	0.037	0.303	0.710
JK23_7	60	1.628	0.135	0.140	0.754	0.065	0.067	4068.174	100.667	103.313	0.592	0.028	0.028	-0.052	0.909
JK23_70	60	1.431	0.091	0.097	0.776	0.052	0.055	4286.431	71.144	74.783	0.705	0.047	0.047	0.503	0.715
JK23_71	60	2.771	0.142	0.156	0.385	0.020	0.022	3493.073	64.814	68.795	0.605	0.031	0.031	0.366	0.654
JK23_72	60	0.625	0.039	0.042	1.766	0.107	0.115	5213.005	71.014	75.058	0.753	0.038	0.039	0.282	0.739
JK23_73	60	2.253	0.159	0.168	0.497	0.034	0.036	3680.729	93.214	96.179	0.600	0.039	0.039	0.249	0.815
JK23_8	60	0.244	0.018	0.019	4.778	0.346	0.364	6353.034	80.349	83.556	0.868	0.026	0.027	0.049	0.918
JK23_9	60	8.430	0.232	0.302	0.120	0.003	0.004	1653.632	45.604	49.336	0.261	0.014	0.014	-0.013	0.776
JK 25															
JK_25_G-1	60	1.915	0.198	0.208	0.672	0.058	0.061	62.566	6.567	6.802	0.672	0.046	0.046	0.170	0.544
JK_25_G-10	60	0.533	0.046	0.048	2.505	0.206	0.218	299.496	25.834	27.190	0.871	0.022	0.022	0.056	0.935
JK_25_G-11	60	1.051	0.078	0.082	1.249	0.109	0.115	142.317	13.102	13.708	0.829	0.018	0.018	-0.053	0.970
JK_25_G-12	60	2.240	0.104	0.118	0.481	0.025	0.029	47.791	3.042	3.329	0.729	0.027	0.027	0.034	0.793
JK_25_G-13	60	2.111	0.084	0.107	0.493	0.018	0.023	51.390	2.089	2.546	0.764	0.026	0.026	0.194	0.405
JK_25_G-14	60	1.310	0.045	0.059	0.787	0.026	0.035	86.940	3.062	3.929	0.807	0.023	0.023	0.337	0.628
JK_25_G-15	60	2.148	0.316	0.333	0.802	0.070	0.073	87.480	8.500	8.853	0.756	0.028	0.028	-0.068	0.949
JK_25_G-16	60	3.861	0.237	0.262	0.305	0.018	0.020	26.023	2.291	2.406	0.593	0.030	0.030	-0.251	0.791
JK_25_G-17	60	1.047	0.083	0.091	1.119	0.070	0.077	125.659	8.083	8.831	0.808	0.024	0.025	0.054	0.800
JK_25_G-18	60	1.011	0.104	0.108	1.658	0.169	0.175	190.519	19.709	20.434	0.828	0.022	0.022	0.001	0.967
JK_25_G-19	60	1.722	0.112	0.120	0.717	0.054	0.058	77.194	6.641	6.991	0.759	0.024	0.024	-0.017	0.876
JK_25_G-2	60	7.986	0.433	0.483	0.134	0.008	0.009	5.589	0.810	0.825	0.286	0.028	0.028	-0.020	0.883
JK_25_G-20	60	4.942	0.321	0.349	0.215	0.014	0.016	14.552	1.181	1.251	0.527	0.049	0.049	0.357	0.181
JK_25_G-21	60	1.105	0.112	0.115	1.429	0.166	0.171	163.521	19.306	19.854	0.843	0.023	0.023	-0.059	0.812
JK_25_G-22	60	1.997	0.159	0.171	0.640	0.045	0.049	66.266	4.990	5.332	0.742	0.020	0.020	-0.078	0.770
JK_25_G-23	60	0.427	0.080	0.081	7.401	1.282	1.300	987.740	198.900	200.856	0.907	0.031	0.031	-0.135	0.992
JK_25_G-24	60	2.098	0.089	0.105	0.511	0.024	0.028	50.268	2.659	3.016	0.721	0.028	0.029	0.139	0.720
JK_25_G-25	60	4.050	0.560	0.590	0.367	0.032	0.034	28.793	3.446	3.541	0.620	0.069	0.069	0.402	0.442
JK_25_G-26	60	1.896	0.119	0.125	0.647	0.055	0.058	69.277	7.226	7.488	0.740	0.026	0.026	-0.076	0.911
JK_25_G-27	60	4.775	0.377	0.398	0.261	0.022	0.024	11.054	1.932	1.957	0.321	0.044	0.044	0.111	0.679
JK_25_G-28	60	1.243	0.065	0.073	0.892	0.049	0.055	100.584	6.054	6.690	0.821	0.025	0.025	0.163	0.818
JK_25_G-29	60	1.197	0.093	0.096	1.187	0.134	0.138	144.311	20.343	20.750	0.812	0.031	0.031	-0.176	0.818
JK_25_G-3	60	5.263	0.371	0.387	0.239	0.023	0.024	19.458	3.819	3.858	0.461	0.032	0.032	0.048	0.408
JK_25_G-30	60	0.217	0.020	0.022	5.577	0.379	0.412	685.606	48.134	51.898	0.899	0.022	0.022	0.104	0.936
JK_25_G-31	60	2.889	0.180	0.196	0.413	0.028	0.030	41.284	3.447	3.640	0.706	0.028	0.028	-0.157	0.890
JK_25_G-32	60	0.724	0.110	0.112	1.666	0.233	0.238	195.268	29.135	29.655	0.853	0.056	0.056	0.165	0.955
JK_25_G-33	60	0.247	0.023	0.024	5.797	0.636	0.657	670.964	66.498	69.155	0.907	0.035	0.035	0.220	0.633
JK_25_G-34	60	0.040	0.005	0.005	-18.136	26.724	26.729	-1546.632	3098.203	3098.512	0.926	0.024	0.024	-0.027	0.988
JK_25_G-35	60	0.493	0.029	0.032	2.226	0.129	0.144	270.931	16.061	17.798	0.897	0.034	0.034	0.291	0.788
JK_25_G-36	60	3.821	0.189	0.223	0.286	0.013	0.016	25.058	1.756	1.894	0.613	0.028	0.028	-0.216	0.579
JK_25_G-37	60	0.173	0.012	0.013	6.951	0.497	0.536	829.276	60.620	65.006	0.888	0.028	0.028	0.128	0.998
JK_25_G-38	60	0.331	0.027	0.029	3.856	0.315	0.334	454.562	36.512	38.712	0.876	0.032	0.032	0.172	0.914
JK_25_G-39	60	0.187	0.022	0.023	10.102	1.427	1.456	1258.963	198.259	201.436	0.879	0.035	0.035	0.020	0.950

JK_25_G-4	60	1.222	0.097	0.104	1.024	0.078	0.083	112.535	9.259	9.791	0.780	0.034	0.034	0.119	0.847
JK_25_G-40	60	0.640	0.088	0.092	2.874	0.283	0.295	343.090	35.255	36.568	0.863	0.034	0.035	-0.087	0.826
JK_25_G-41	60	0.541	0.092	0.094	4.931	0.647	0.663	590.243	78.288	80.050	0.867	0.035	0.036	-0.155	0.956
JK_25_G-42	60	0.626	0.069	0.069	2.405	0.643	0.646	273.871	66.392	66.843	0.863	0.057	0.057	0.051	0.990
JK_25_G-43	60	4.758	0.245	0.280	0.230	0.012	0.013	15.146	0.960	1.052	0.499	0.029	0.029	0.253	0.659
JK_25_G-44	60	4.490	0.343	0.359	0.283	0.027	0.028	18.609	1.933	2.004	0.548	0.056	0.056	0.581	0.076
JK_25_G-45	60	0.618	0.047	0.049	2.362	0.268	0.276	291.166	36.456	37.377	0.851	0.022	0.022	-0.114	0.965
JK_25_G-46	60	0.235	0.016	0.017	4.902	0.318	0.348	623.307	41.952	45.512	0.938	0.032	0.032	0.874	0.909
JK_25_G-5	60	5.151	0.350	0.374	0.236	0.018	0.019	16.828	2.045	2.100	0.476	0.039	0.039	-0.324	0.471
JK_25_G-6	60	1.352	0.141	0.143	1.291	0.196	0.199	138.765	20.177	20.556	0.832	0.051	0.051	0.093	0.946
JK_25_G-7	60	0.059	0.015	0.015	-3.632	15.807	15.807	-1679.751	2242.776	2243.281	0.885	0.024	0.024	0.012	0.972
JK_25_G-8	60	0.695	0.054	0.057	1.880	0.149	0.158	213.909	17.969	18.962	0.830	0.019	0.019	-0.185	0.949
JK_25_G-9	60	3.479	0.338	0.351	0.426	0.045	0.046	43.017	5.694	5.823	0.622	0.032	0.032	-0.116	0.738
GQ6-2 matrix															
GQ6_2_matrix-1	60	1.543	0.029	0.048	0.651	0.012	0.019	4016.271	19.802	29.787	0.575	0.009	0.010	0.320	0.673
GQ6_2_matrix-10	60	1.413	0.035	0.048	0.719	0.018	0.025	4198.485	23.550	32.293	0.629	0.010	0.011	0.331	0.811
GQ6_2_matrix-11	60	0.935	0.017	0.029	1.074	0.018	0.031	4721.092	16.673	28.246	0.705	0.011	0.012	0.483	0.616
GQ6_2_matrix-12	60	0.978	0.020	0.031	1.032	0.022	0.033	4664.534	19.615	30.058	0.699	0.011	0.012	0.486	0.664
GQ6_2_matrix-13	60	1.076	0.026	0.036	0.935	0.022	0.031	4523.041	27.446	35.565	0.667	0.013	0.014	0.227	0.613
GQ6_2_matrix-14	60	1.102	0.029	0.039	0.926	0.024	0.033	4502.943	25.484	34.300	0.666	0.012	0.013	0.417	0.731
GQ6_2_matrix-15	60	1.174	0.026	0.037	0.859	0.019	0.028	4421.041	21.445	31.144	0.661	0.016	0.016	0.558	0.453
GQ6_2_matrix-16	60	1.364	0.029	0.043	0.734	0.015	0.023	4184.261	19.914	29.523	0.603	0.012	0.013	0.545	0.584
GQ6_2_matrix-17	60	1.342	0.053	0.063	0.781	0.029	0.034	4206.148	29.771	37.067	0.594	0.017	0.017	0.638	0.657
GQ6_2_matrix-18	60	1.396	0.034	0.048	0.728	0.017	0.024	4169.650	24.414	33.819	0.606	0.010	0.011	0.308	0.755
GQ6_2_matrix-19	60	1.458	0.031	0.046	0.694	0.014	0.022	4104.284	20.610	30.700	0.597	0.010	0.011	0.376	0.681
GQ6_2_matrix-2	60	1.547	0.038	0.053	0.658	0.016	0.022	4011.508	28.734	36.571	0.571	0.010	0.011	0.049	0.803
GQ6_2_matrix-20	60	1.320	0.031	0.044	0.768	0.018	0.025	4287.511	24.090	33.257	0.643	0.011	0.011	0.344	0.735
GQ6_2_matrix-21	60	1.569	0.042	0.057	0.648	0.016	0.022	4034.728	24.871	34.261	0.588	0.012	0.012	0.084	0.763
GQ6_2_matrix-22	60	1.422	0.033	0.047	0.711	0.016	0.023	4173.002	21.150	30.852	0.619	0.013	0.013	0.498	0.609
GQ6_2_matrix-23	60	1.300	0.036	0.049	0.780	0.020	0.027	4260.102	28.681	36.059	0.615	0.016	0.017	0.421	0.558
GQ6_2_matrix-24	60	1.426	0.034	0.048	0.712	0.017	0.024	4170.581	27.469	35.747	0.618	0.012	0.013	0.236	0.673
GQ6_2_matrix-25	60	1.369	0.039	0.050	0.745	0.021	0.028	4218.081	31.727	39.270	0.625	0.014	0.015	0.283	0.740
GQ6_2_matrix-26	60	1.370	0.040	0.051	0.746	0.023	0.029	4229.575	30.452	37.985	0.632	0.017	0.017	0.265	0.646
GQ6_2_matrix-27	60	1.395	0.039	0.052	0.732	0.020	0.026	4198.959	30.920	38.291	0.620	0.014	0.015	0.330	0.648
GQ6_2_matrix-28	60	1.599	0.036	0.053	0.631	0.014	0.020	3953.886	23.500	32.325	0.559	0.011	0.012	0.402	0.560
GQ6_2_matrix-29	60	1.372	0.030	0.043	0.738	0.017	0.024	4193.144	25.284	34.517	0.614	0.013	0.013	0.352	0.596
GQ6_2_matrix-3	60	1.571	0.033	0.049	0.641	0.014	0.020	3955.635	21.907	31.484	0.551	0.010	0.011	0.454	0.597
GQ6_2_matrix-30	60	1.503	0.035	0.050	0.672	0.016	0.022	4071.117	29.688	37.388	0.592	0.014	0.015	0.297	0.586
GQ6_2_matrix-31	60	1.505	0.038	0.051	0.674	0.017	0.023	4074.233	28.232	36.128	0.594	0.012	0.013	0.360	0.673
GQ6_2_matrix-32	60	1.392	0.031	0.045	0.728	0.016	0.024	4167.172	25.283	33.853	0.602	0.012	0.012	0.299	0.684
GQ6_2_matrix-33	60	1.400	0.038	0.051	0.731	0.019	0.026	4155.487	31.526	38.937	0.595	0.012	0.013	0.189	0.740
GQ6_2_matrix-34	60	1.249	0.028	0.041	0.808	0.018	0.026	4341.026	23.977	32.429	0.647	0.015	0.015	0.388	0.581
GQ6_2_matrix-35	60	1.133	0.024	0.036	0.890	0.020	0.029	4490.149	24.204	33.288	0.680	0.011	0.011	0.279	0.788
GQ6_2_matrix-36	60	1.302	0.033	0.046	0.779	0.018	0.026	4312.078	21.995	31.285	0.649	0.013	0.014	0.559	0.595
GQ6_2_matrix-37	60	1.249	0.030	0.043	0.810	0.019	0.027	4336.396	25.754	34.141	0.638	0.013	0.013	0.350	0.678
GQ6_2_matrix-38	60	1.312	0.029	0.042	0.770	0.017	0.025	4268.662	25.270	34.125	0.631	0.011	0.012	0.265	0.743
GQ6_2_matrix-39	60	1.471	0.033	0.048	0.689	0.016	0.022	4108.596	24.873	33.317	0.602	0.012	0.013	0.357	0.648
GQ6_2_matrix-4	60	1.654	0.038	0.054	0.612	0.014	0.020	3901.658	27.257	35.306	0.547	0.009	0.010	0.165	0.748
GQ6_2_matrix-40	60	1.458	0.031	0.046	0.695	0.015	0.022	4135.909	20.960	31.069	0.608	0.009	0.010	0.472	0.686
GQ6_2_matrix-41	60	1.319	0.028	0.043	0.763	0.015	0.024	4276.784	20.931	30.873	0.636	0.011	0.012	0.445	0.688
GQ6_2_matrix-42	60	1.281	0.028	0.041	0.791	0.017	0.025	4319.626	22.580	31.895	0.644	0.012	0.013	0.344	0.624
GQ6_2_matrix-43	60	1.355	0.029	0.043	0.746	0.016	0.024	4223.144	24.105	33.774	0.619	0.011	0.012	0.346	0.643
GQ6_2_matrix-44	60	1.404	0.028	0.044	0.715	0.014	0.022	4142.896	20.671	30.864	0.593	0.011	0.011	0.405	0.619
GQ6_2_matrix-45	60	1.456	0.038	0.051	0.701	0.018	0.024	4130.814	27.816	35.872	0.606	0.012	0.012	0.284	0.737
GQ6_2_matrix-46	60	1.384	0.034	0.047	0.736	0.018	0.025	4192.871	26.198	35.052	0.611	0.012	0.012	0.340	0.701
GQ6_2_matrix-47	60	1.325	0.032	0.045	0.768	0.018	0.026	4281.220	24.335	33.524	0.642	0.012	0.013	0.369	0.702
GQ6_2_matrix-48	60	1.178	0.030	0.042	0.863	0.021	0.029	4413.838	26.630	34.945	0.649	0.013	0.014	0.404	0.658
GQ6_2_matrix-49	60	1.499	0.037	0.051	0.677	0.017	0.023	4086.574	25.566	34.518	0.601	0.012	0.012	0.347	0.646
GQ6_2_matrix-5	60	1.530	0.031	0.049	0.659	0.013	0.020	4021.685	22.905	31.968	0.572	0.010	0.010	0.269	0.691
GQ6_2_matrix-50	60	1.426	0.038	0.051	0.709	0.019	0.025	4120.229	33.959	40.823	0.591	0.013	0.014	0.155	0.777
GQ6_2_matrix-51	60	1.543	0.041	0.056	0.662	0.017	0.023	4047.218	27.391	35.111	0.590	0.014	0.015	0.417	0.591
GQ6_2_matrix-52	60	1.441	0.038	0.051	0.708	0.018	0.025	4146.619	24.647	33.263	0.605	0.012	0.013	0.423	0.689
GQ6_2_matrix-53	60	1.461	0.030	0.047	0.692	0.014	0.021	4111.364	23.286	32.798	0.598	0.011	0.012	0.207	0.686
GQ6_2_matrix-54	60	1.504	0.026	0.045	0.669	0.012	0.020	4063.797	19.046	29.442	0.587	0.010	0.011	0.396	0.558
GQ6_2_matrix-55	60	1.324	0.031	0.044	0.765	0.018	0.025	4286.621	24.035	32.813	0.645	0.011	0.011	0.279	0.757
GQ6_2_matrix-6	60	1.644	0.038	0.056	0.617	0.013	0.020	3916.202	22.941	32.161	0.553	0.009	0.010	0.356	0.749
GQ6_2_matrix-7	60	1.548	0.037	0.052	0.656	0.015	0.022	4004.402	24.101	32.982	0.567	0.009	0.009	0.319	0.798
GQ6_2_matrix-8	60	1.338	0.027	0.043	0.753	0.015	0.023	4235.006	22.925	32.787	0.619	0.010	0.011	0.252	0.709
GQ6_2_matrix-9	60	1.404	0.029	0.044	0.718	0.015	0.022	4195.808	23.719	32.560	0.627	0.009	0.010	0.151	0.812